ADVANCING EARTH AND SPACE SCIENCES

JGR Space Physics

RESEARCH ARTICLE
10.1029/2024JA032635

Assessing the Sources of the O^+ in the Plasma Sheet

J. Liao[1], **L. M. Kistler**[1], **C. G. Mouikis**[1], **S. A. Fuselier**[2,3], **and M. Hedlund**[1]

[1]Department of Physics and Space Science Center, University of New Hampshire, Durham, NH, USA, [2]Southwest Research Institute, San Antonio, TX, USA, [3]University of Texas at San Antonio, San Antonio, TX, USA

Key Points:

- Cusp-source O^+ is observed entering the plasma sheet (PS) from the lobe throughout the <25 R_E magnetotail
- The nightside auroral-source O^+ is identified at <100 eV inside 10 R_E, with a more energetic component further out on the duskside
- We estimate that during quiet times, the dayside cusp contributes the most to the near-earth PS O^+

Correspondence to:

J. Liao,
jing.liao@unh.edu

Citation:

Liao, J., Kistler, L. M., Mouikis, C. G., Fuselier, S. A., & Hedlund, M. (2024). Assessing the sources of the O^+ in the plasma sheet. *Journal of Geophysical Research: Space Physics*, *129*, e2024JA032635. https://doi.org/10.1029/2024JA032635

Received 13 MAR 2024
Accepted 29 JUL 2024

Abstract

To study the average contributions of the cusp outflow through the lobes and of the nightside auroral outflow to the O^+ in the plasma sheet (PS), we performed a statistical study of tailward streaming O^+ in the lobes, plasma sheet boundary layer|the plasma sheet boundary layer (PSBL) and the PS, using MMS/Hot Plasma Composition Analyzer (HPCA) data from 2017 to 2020. Similar spatial patterns illustrate the entry of cusp-origin O^+ from the lobes to the PS through the PSBL. There is an Y_{GSM}-dependent energy pattern for the lobe O^+, with low-energy O^+ streaming closer to the tail center and high energy (1–3 keV) O^+ streaming near the flanks. Low energy (1–100 eV) O^+ from the nightside auroral oval is identified in the near-Earth PSBL/PS with high-density (>0.02 cm^{-3}), and energetic (>3 keV) streaming O^+ with similar density (~0.013 cm^{-3}) is observed further out on the duskside of the PSBL/PS. The rest of the nightside auroral O^+ in the PSBL is mixed with O^+ coming in from the lobe, making it difficult to distinguish the source. We estimated the contributions of the different sources of H^+ and O^+ ions through the PS between 7 and 17 R_E, using estimates from this work and data extracted from previous studies. We conclude that, during quiet times, the majority of the near-Earth PS H^+ are from the cusps, the polar wind and Earthward convection from the distant tail. Similarly, while the O^+ in the same region has a mixed source, cusp origin outflow provides the highest contribution.

Plain Language Summary

We studied the sources of the plasma sheet (PS), using MMS/HPCA data. We observed and mapped the location of the oxygen ions streaming from the dayside cusp region entering the PS through the plasma sheet boundary layer (PSBL). The observations of the oxygen ions from the nightside auroral oval streaming inside PSBL show that this population has higher density than the dayside cusp origin oxygen ions. We estimated the number of the proton and oxygen ions per second entering and leaving the PS and conclude that during quiet times, the solar wind protons are the major source for PS population and ionospheric oxygen ions from dayside cusp is the major source for oxygen ions in the PS.

1. Introduction

The Earth's magnetosphere contains ion populations from both the solar wind and ionosphere. Heavy O^+ ions, originating from the ionosphere, can dominate the ring current energy density during geomagnetic storm times. Energetic O^+ ions in the plasma sheet (PS) directly impact the storm time ring current O^+ content. Previous studies (Keika et al., 2013; Kistler et al., 1989; Kistler et al., 2016) show that adiabatic inward transport of the hot PS population at ~6 R_E contributes to the dominant pressure that drives the storm time ring current. Thus, understanding this near-Earth hot PS population is one of the keys to predicting the strength of the ring current.

Comparisons between the PS composition at 15–20 R_E (Mouikis et al., 2010) and around 6 R_E (Kistler & Mouikis., 2016) show that the O^+/H^+ ratio increases with decreasing radial distance. One explanation is that there may be significant entry of O^+ to the PS closer to the Earth. There are two sources for the direct entry of energetic O^+ to the PS: the cusp and the nightside aurora. The significant entry near the Earth could be from either or both sources. Polar wind can be another source for streaming O^+ at very low energies (Yao et al., 2021). The velocity filter effect leads to a separation of O^+ and H^+ in the lobe due to their different velocities (called the geomagnetic mass spectrometer) that may also impact the radial dependence of different ion species entering the near-Earth PS (Chappell et al., 1987).

Ions outflowing from the dayside cusp region move across the polar caps and travel along the open field lines in the lobes, with the convection from the dawn-dusk magnetospheric electric field moving them toward the central current sheet. While some ions are lost in the distant tail, others may enter the PS during tail reconnection and convect Earthward. Moore et al. (2005) showed the difference between entry of ions near the Earth and further down the tail. Ions with lower energy (<1 keV) may reach the PS close to the Earth, where the field is close to

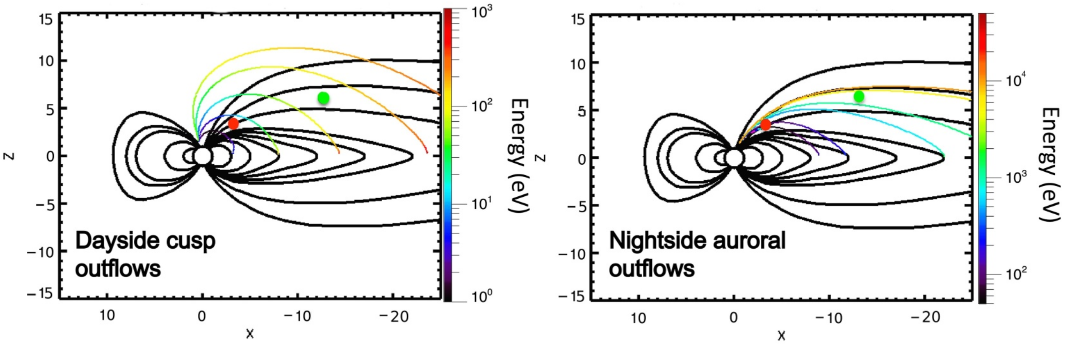

Figure 1. Simulated velocity filter effect for ions from dayside cusp and nightside aurora. Adapted from Kistler et al. (2019).

dipolar. Those ions will remain close to field-aligned and mirror while drifting eastward with little energy gain, contributing to the warm plasma cloak. If the ions are more energetic (>1 keV), they may reach the PS further down the tail where the PS is stretched. Those ions will then be scattered, heated, becoming part of the hot isotropic PS. The behavior depends on the particle gyroradius, compared to the curvature of the neutral sheet. At 15–19 RE, the Cluster spacecraft observed the cusp origin ions entering the PS far enough down the tail to become isotropic and heated, becoming part of the hot PS (e.g., Kistler et al., 2010). During storm times, the intensity of cusp source ions increases, and the entry into the PS may last for many hours. Ionospheric ions from the nightside auroral region travel along the closed field lines and may enter the PS through plasma sheet boundary layer|the plasma sheet boundary layer (PSBL). This outflow is usually bursty. The intensity varies both with substorms and storms. Lower energy ions enter the PS near the Earth, and remain at low energy, while higher energy ions enter further down the tail, and may become isotropic, heated, and become part of the hot PS.

Adapted from Kistler et al. (2019), Figure 1 shows the trajectories of particles with different initial energies from the two different outflow regions. For both regions, when the ions of different energies flow out from the source, they are convected toward the center at the same speed. As a result, the trajectories of ions are separated due to their initial energies, with energetic ions reaching further down the tail and low-energy ions trapped near the Earth. Dayside cusp origin ions move along the open field lines, become dispersed, and gain energy from centrifugal acceleration as they move out. Nightside aurora origin ions following closed field lines are also dispersed by energy as they enter the PS. As a result, in the in situ observations, spatial difference will lead to an energy difference.

Ionospheric outflow from both the dayside cusp and nightside auroral region increases during geomagnetic active time (Kistler et al., 2006; Moore, Chandler, et al., 1999; Nosè et al., 2003). The transport path of the O^+ is also strongly affected by geomagnetic activity (Liao et al., 2010). Enhanced convection during geomagnetic storms can lead to stronger centrifugal acceleration for the cusp outflowing O^+ and leading to more energetic O^+ inside the lobes (Cladis, 1986; Huddleston et al., 2005; Kistler et al., 2019). Substorm-associated reconnections in the tail can bring more O^+ into the PS and lead to stronger Earthward convection than quiet times.

The enhancement of ionospheric outflow has been found to be strongly correlated with the solar wind drivers, in particular pressure and velocity (Cully et al., 2003; Elliott et al., 2001; Moore, & Chandler et al., 1999). The solar wind pressure and velocity also affect the O^+ transport path inside the lobes through convection field (Liao., 2011). Increased EUV leads to stronger ionospheric outflow on both dayside and nightside (Strangeway et al., 2005; Zhao et al., 2020, 2022).

The tailward moving, field-aligned O^+ observed in the lobes is mostly from the dayside cusp. Liao et al. (2010) studied the transport path of ionospheric O^+ from the dayside cusp with Cluster lobe observations. The study showed that O^+ ions from the dayside cusps are commonly observed in the lobes even during non-storm times. The occurrence rate of O^+ is even higher during storm time. There is an IMF By-driven asymmetry on the transport path of cusp origin O^+, which is strongest when IMF By is positive.

The tailward moving, field-aligned O^+ in the PSBL and PS could come from either dayside cusp or nightside auroral oval. In this paper, we present a statistical study of the O^+ entry into the PSBL and the PS: the spatial distribution of the observed ions, their energy and density distribution, and how their distribution varies

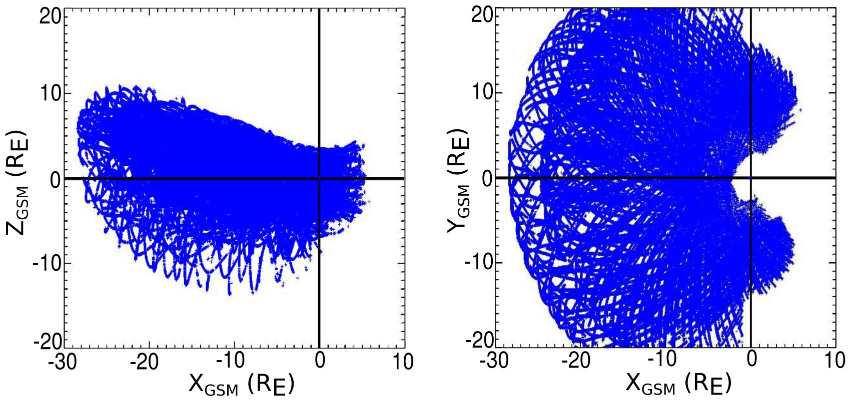

Figure 2. 2017–2020 orbital segments of MMS within the magnetosphere, in XZ_{GSM}, XY_{GSM} projection. Dayside observation is taken out.

depending on the driver. We will also discuss the average (mainly non-storm time) supply and loss of ions in the near-Earth PS.

2. Data and Methods

2.1. Spacecraft

The Cluster satellites have provided good measurements of O^+ in the lobe, but due to their polar orbit, there are fewer equatorial PS measurements from -6 to -15 R_E. Complementary to Cluster's lobe observations, Magnetospheric Multiscale (MMS) spacecraft spent extended time orbiting near the central PS region, which allows us to perform a statistical study of O^+ entry into the PS through the PSBL and the nightside entry of the O^+ from the nightside auroral source.

The MMS Mission was launched on 13 March 2015, to study the Earth's magnetosphere, using four identical spacecraft flying in a tetrahedral formation. We use the MMS data from 2017 to 2020 which covers orbital distances out to 28 R_E. Figure 2 shows the orbital segments from 2017 to 2020 in XZ_{GSM}, and XY_{GSM} planes. The focus of the orbits is within the equatorial plane: orbits are confined within +/− 10 R_E in Z_{GSM}, providing great PSBL and PS coverage. The full coverage is not symmetrical between the north and south hemispheres, but orbit coverage between +/− 5 R_E is symmetrical enough for spatial distribution analysis. The orbits cover both positive and negative Y_{GSM} regions (dawn and dusk sides of the magnetosphere). We will not use the data collected on the dayside (MLT between 8 and 16) and outside $|Y_{GSM}| = 20$ R_E

MMS spacecraft are close to each other, and because we average data over 5 min for better statistics, the data used in this study are essentially the same on different spacecraft for our purpose. Thus, we only used data collected by MMS1 in this study.

2.2. Instrument

Onboard each MMS spacecraft, the Hot Plasma Composition Analyzer (HPCA) (Young et al., 2016) is an instrument combining an electrostatic energy analyzer with a carbon-foil based time-of-flight analyzer. It measures the flux of H^+, He^{++}, He^+, and O^+ from 1 eV to 40 keV at 16 elevation anodes, with a time resolution of 10–15 s (Young et al., 2016). This study predominantly uses HPCA fast Survey data, which sums the distribution into 8 elevation and 8 azimuthal angular bins, and 16 energy bins. The magnetic field used in this study is collected by Fluxgate Magnetometers (FGM) (Torbert et al., 2016). IDL Software based on the SPEDAS/TDAS package is used to extract data. We calculated the density of the streaming O^+ around its energy peak and pitch angle direction. The impact of spacecraft potential should be less than 10 eV (Goldstein et al., 2023).

2.2.1. Compression Scheme Modes

For onboard memory usage optimization, HPCA data are collected under Survey, Fast and Burst modes (Young et al., 2016). The Fast or Survey data streams are collected nearly continuously. The Burst mode data stream is collected concurrently with the collection of Fast or Survey mode data but at a higher energy and angular resolution. All data collected in Fast, Survey or Burst modes are downlinked to the ground after a "lossy" compression algorithm is applied. The "lossy" compression operated continuously from the beginning of the mission. It was temporarily turned off under Fast Survey mode from 2018-05-27 to 2018-09-25 and for the entire 2019 tail season from 2019-04-16 to 2019-08-17. The lossy scheme was permanently turned off after 2022-05-24.

The onboard "lossy" compression scheme employed by HPCA on MMS drops the least significant bit in any accumulated energy-angle-angle bin for each species before downlinking the data to the ground (Young et al., 2016). Therefore, in Fast and Survey modes, for each 16 energy—8 azimuth-angle—8 elevation-angle matrix accumulated over a ½ spin, any bins with single counts are eliminated. This can result in significantly lower fluxes for the minor species and/or low energy populations, where single counts in each energy-angle-angle bin are observed more frequently. It should be emphasized that the impact is greater for isotropic populations at all energies where counts are equally spread over all angular bins, compared to anisotropic populations for the same total number of counts where the counts are concentrated in a smaller number of angular bins. In Burst mode the energy-angle-angle resolution is higher (64 energy—16 azimuth-angle—16 elevation-angle). Therefore, for each bin in a Fast/Survey mode matrix there are 16 corresponding bins in Burst mode and therefore counts will be spread over 16 bins instead. In Burst mode the impact of the compression is even greater since the counts in one survey mode energy-angle-angle bin are spread over 16 bins, resulting in a much higher probability that single counts being dropped.

As our study focuses on field-aligned O^+, which can be a relatively minor species, with low flux particularly at low energies, the lossy scheme had a significant impact on the data. In particular, it resulted in significant loss of O^+ in the lower energy range. To aggregate all the data from 2017 to 2020, including both compressed and non-compressed times, we analyzed the impact of the compression scheme on the occurrence frequency, median and minimum energy, and median density. We simulated the effect of the compression algorithm on the data collected when the compression scheme was off in 2018–2019.

For occurrence frequency, we compared the occurrence frequency maps with and without the compression and calculated empirical occurrence frequency correction factors to restore the occurrence frequency to the original level (see Appendix A). All occurrence frequency results shown in this study are after the correction.

For the streaming O^+ median and minimum energy analysis, we studied the compression scheme's impact on the median and minimum energy maps in all regions. The median value of the energy is higher when the data is compressed. The increase is smallest for lobes and higher for PSBL and the highest in the PS. However, the general patterns remain for the median energy maps for all regions. The conclusions are the same for the minimum energy maps. While we can use a region-related factor to correct the occurrence frequency, the impact of the compression scheme on the energy profile is more non-linear and difficult to compensate for. In the following sections, we present the median and minimum energy maps with the compressed data and uncompressed data after compression simulation to have a consistent data set. The maps show the energy slightly higher than the actual value in median and minimum energy maps, but the general pattern of the maps remains the same.

The median density maps are the median value of densities of all the observed streaming O^+ in each bin. The compression scheme has minimal effect on the median density maps because the streaming O^+ is strongly anisotropic, concentrated in relatively few angular bins. Details of the compression scheme impact can be found in Appendix A.

2.3. Auto Identification of Streaming O^+ for MMS

To study the transport path and entry of the ionospheric ions, we must first identify the O^+ from the dayside cusp or nightside aurora region traveling in different regions within the magnetosphere. Our goal is to identify the populations before they have become scattered and isotropized in the PS, which makes their source much more difficult to identify. To achieve this, we study the continuous outward/tailward moving, field-aligned populations, which we call "streaming O^+." Due to the velocity filter effect, ions from both ionospheric sources will separate according to their velocity (Chappell et al., 1987). As a result, we often observe streaming O^+ as a mono-energetic population with a strong flux in the energy spectra.

Previously, Liao et al. (2010) implemented an algorithm to identify the streaming O^+ automatically using Cluster data in the lobes where the streaming O^+ is close to mono-energetic and tailward moving. In this study, we are

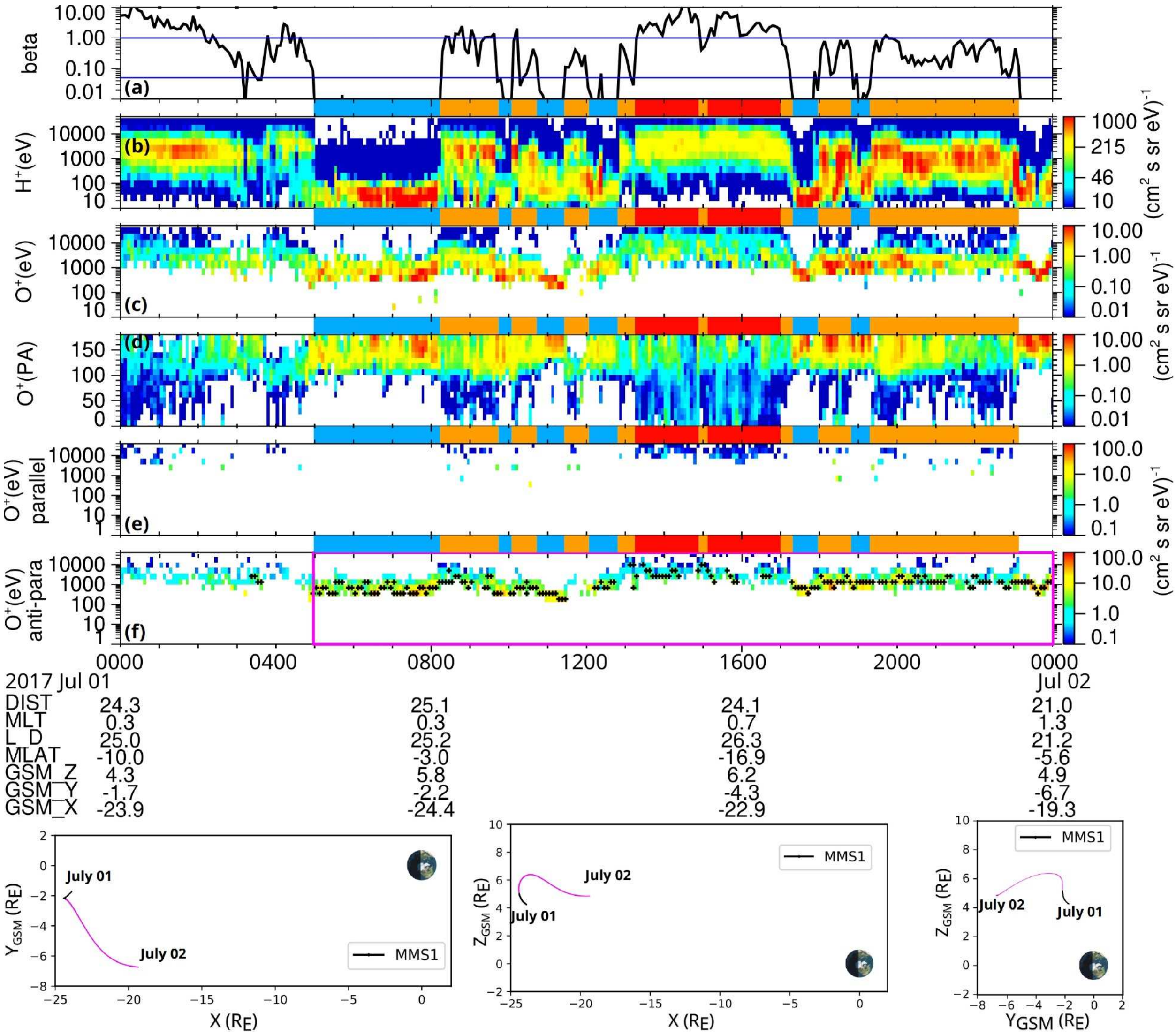

Figure 3. Observations of streaming O^+ from the dayside cusp. Panels from top to bottom: Panel (a) is plasma beta. Panel (b) is proton energy spectra over all angles. Panel (c) is O^+ energy spectra over all angles. Panel (d) is the pitch angle of O^+ at all energy. Panel (e) is the energy spectra of parallel O^+ with pitch angle between 0 and 60 degrees. Panel (f) is the energy spectra of antiparallel O^+ with pitch angle between 120 and 180 degrees. Black dots in panel (f) show the identified streaming O^+. Bars between the energy spectra indicate the regions of the satellite: blue means lobe, orange means PSBL, and red means the plasma sheet. MMS orbits are shown in projections of XY_{GSM}, XZ_{GSM} and YZ_{GSM} at the bottom of the figure.

targeting a similar population but in different regions. First, as MMS is near/inside the PS, there can be multiple streaming populations at different energies and directions. Second, we would like to identify the freshly outflowing populations, not a bouncing, bidirectional field-aligned population. Thus, we have modified the algorithm to accommodate the HPCA data collected in different regions covered by the MMS orbits. We start by averaging data for 5 min to increase the statistics of the data.

To capture streaming O^+ in both parallel and antiparallel directions, we calculate the energy spectra for O^+ with pitch angle between 0 and 60° (parallel) and between 120 and 180° (antiparallel). To remove isotropic and mirroring (bidirectional) populations, we subtract the flux, for each energy, of antiparallel O^+ energy spectra from the parallel ones, and vice versa. Any negative values will be considered as zero. An example is shown in Figure 3, where panels (b) and (c) show the OMNI-directional energy spectra for H^+ and O^+, and panels (e) and (f) show the parallel and anti-parallel spectra after subtraction of the bi-directional or isotropic contributions. Then energy peaks are identified for each direction. For each energy peak, we calculated the pitch angle spectra for O^+ ions collected around the energy peak, so we can study the pitch angle distribution of the targeted streaming O^+ population. The pitch angle is partial depending on whether the energy spectra is parallel or anti-parallel. By reviewing the pitch angle spectra, we can identify the potential streaming O^+ population by their clear pitch angle peak. To ensure the continuity of the streaming population, we require the streaming population to continue for more than three-time segments within the same or adjacent energy bin and pitch angle peak bin. The black marks in the last panel of Figure 3 show the identification results, which we will discuss again in session 3. More details of the identification algorithm can be found in Liao et al. (2010).

3. Streaming O^+

3.1. Observations of Streaming O^+

Figures 3–5 present examples of observed streaming O^+ populations. Figure 3 shows an example of a typical streaming O^+ event observed by MMS in the lobes, the PSBL, and the PS on 1 July 2017. This is an example of the cusp-source ions coming in from the lobes to the PSBL and then into the PS, as has been shown in Kistler et al. (2010). The panels (a–d) are plasma β, H^+ energy spectra, O^+ energy spectra, O^+ pitch angle spectra. Panel (e) and (f) are the parallel and antiparallel energy spectra after subtraction described in method Section 2.3. The black marks in the last panel show the identified streaming O^+. The lack of black marks in panel (e) indicates that there is no parallel steaming O^+ identified. Bars between the panels indicate the regions of the satellite: blue means lobe, orange means PSBL, and red means the PS. The region identification is done using the plasma β. The Plasma β is calculated using the sum of the local proton and oxygen pressure divided by magnetic pressure. Using the plasma β, we divide the region into lobe ($\beta < 0.05$), PSBL ($\beta > 0.05$ and $\beta < \beta 1$), and the PS ($\beta > \beta 1$) (Adapted from Miyashita et al. (2020)). $\beta 1$ is defined as

$$\beta 1 = 1 \qquad \text{at } R \geq 15\ \mathrm{R_E}$$

$$\mathrm{Log}(\beta 1) = 0.14R - 2.1 \qquad \text{at } R < 15\ \mathrm{R_E}$$

Where $R = \sqrt{X2 + Y2}$

In Figure 3, from 05:00 to 08:00, a streaming O^+ population at around 1 KeV is observed in lobes shown as the yellow/red band in the O^+ energy spectra (panel c). In the O^+ pitch angle spectra (panel d), we can see this high flux population is mostly field aligned in the antiparallel direction. During the observation time, MMS is in the northern hemisphere, so the observed anti-parallel streaming heavy ions are outflowing from the source. A similar streaming population is observed in the H^+ spectra with a lower energy (<100 eV) that is roughly 16 times lower than the streaming O^+, implying that ions of different species are grouped/separated by their velocities. After 08:00, the spacecraft moves in and out between the lobes and the PSBL due to the dynamic movement of the magnetosphere, and the streaming O^+ is observed during the whole time. Eventually at ~13:20, the MMS enters the PS. The intense flux of the streaming population makes it stand out from the background population in the lobes and the PSBL. The flux becomes less intense when the ions enter the PS, get scattered and become isotropic, and the energy increases, implying possible acceleration during the entry. Similar characteristics have been observed and discussed in Kistler et al. (2010). MMS/HPCA observes the streaming O^+ population during the whole PS encounter and continues to observe it as the satellite leaves the PS and goes back into the lobe/PSBL regions. No streaming O^+ is observed in the parallel direction, confirming that the heavy ions are the outflowing population. During the observation time, the magnetosphere is quiet, with Kp index peaking at 3 and the lowest Dst index is −13 nT.

Figure 4 shows an example observation of energetic streaming O^+ observed in the lobe region near the magnetosheath. The panels are in the same arrangement as in Figure 3. At the start of the 2019-10-25, the satellite was in the sheath, indicated by the high plasma beta, and the strong proton flux over a wide energy range. Due to the background contamination of the O^+ from the high H^+ rates during this time, the O^+ data have been removed. At around 05:00, MMS enters the lobe where it remains until 16:00, except for brief excursions to the PSBL. As marked by the black marks in Figure 4e, streaming O^+ is observed for most of the time that MMS is in the lobe. At the bottom of Figure 4 the orbits of the MMS during the observation time are shown, with the pink part of the orbit matching the pink box in panel (e). The YZ_{GSM} orbit plot shows that during the observation time of the lobe streaming O^+, the Z_{GSM} ranges from −5 to −9 R_E, which is a typical southern lobe region, and Y_{GSM} ranges from 10 to 20 R_E, which is on the dusk flank near the sheath. X_{GSM} is near −10 R_E the whole time. The streaming O^+ is

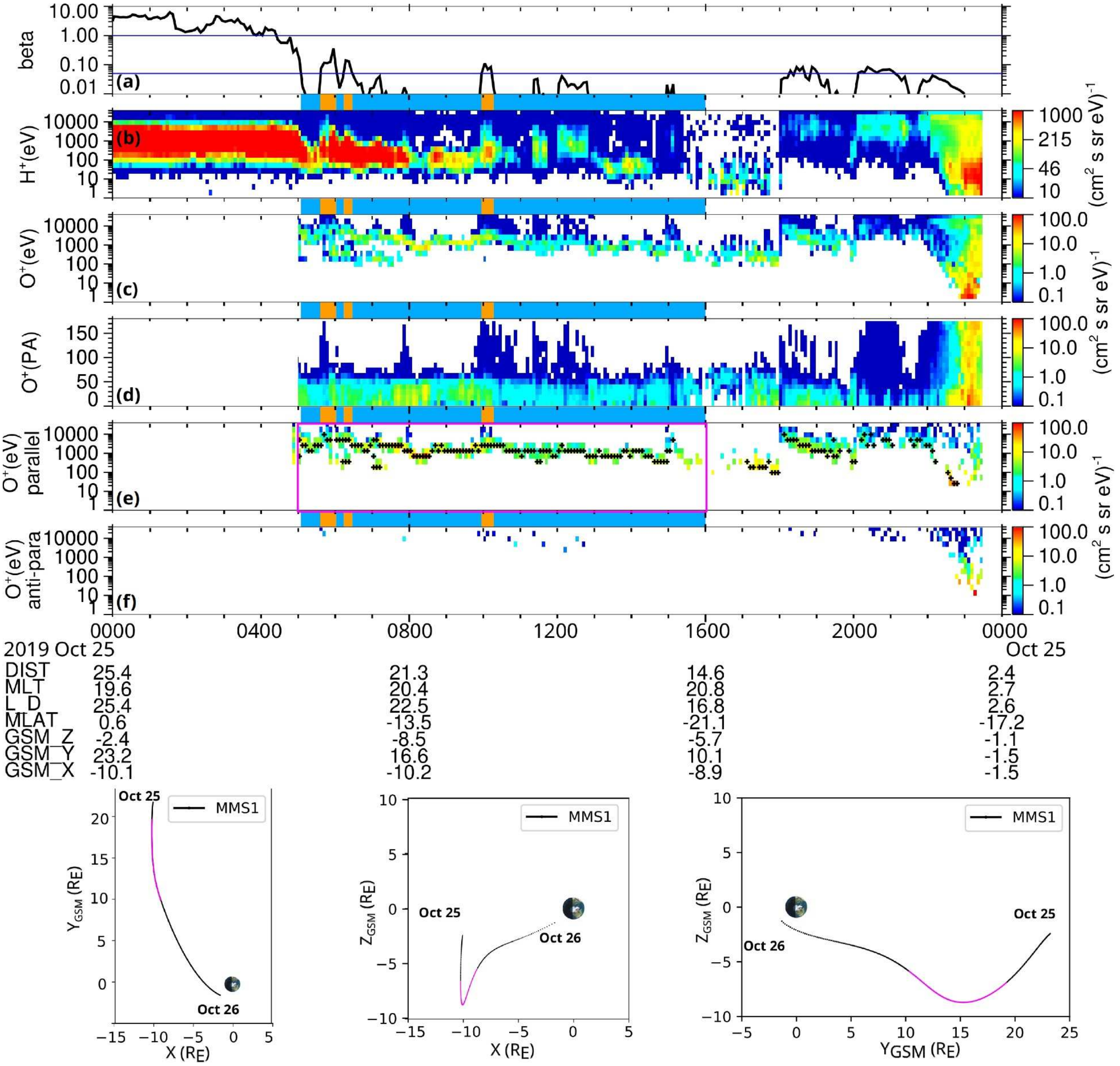

Figure 4. Observations of energetic streaming O^+ near the flanks. Panels from top to bottom: Panel (a) is plasma beta. Panel (b) is proton energy spectra over all angles. Panel (c) is O^+ energy spectra over all angles. Panel (d) is the pitch angle of O^+ at all energy. Panel (e) is the energy spectra of parallel O^+ with pitch angle between 0 and 60 degrees. Panel (f) is the energy spectra of antiparallel O^+ with pitch angle between 120 and 180 degrees. Black dots in panel (e) show the identified streaming O^+. Bars between the energy spectra indicate the regions of the satellite: blue means lobe and orange means B_L. MMS orbits are shown in projections of XY_{GSM}, XZ_{GSM} and YZ_{GSM} at the bottom of the figure.

very energetic (>300 eV) during the observation, and the energy is higher when Y_{GSM} is larger. The highest observed streaming population is at 5 KeV when Y_{GSM} is around -19 R_E. We will discuss those energetic lobe streaming O^+ observed near the flank area again in Section 4.4.

Figure 5 shows an example observation of nightside auroral outflows on 2020-10-27. The left panels are in the same arrangement as in Figures 3 and 4 but without plasma beta panel. The three panels on the right show the orbit of the MMS during the observation in XY_{GSM}, XZ_{GSM} and YZ_{GSM} projections. The pink segment of the orbit corresponds to the observation time of the pink box in panel (d). MMS moves from $X_{GSM} = -8$ R_E toward the Earth, till X_{GSM} is less than -2 R_E, and from the southern hemisphere at around $Z_{GSM} = -7$ R_E toward the equatorial plane near $Z_{GSM} = -1$ R_E. During the whole observation time, MMS is on the nightside of the Earth. Starting from 07:50, MMS detects clear outflowing (parallel streaming in southern hemisphere) O^+, and then

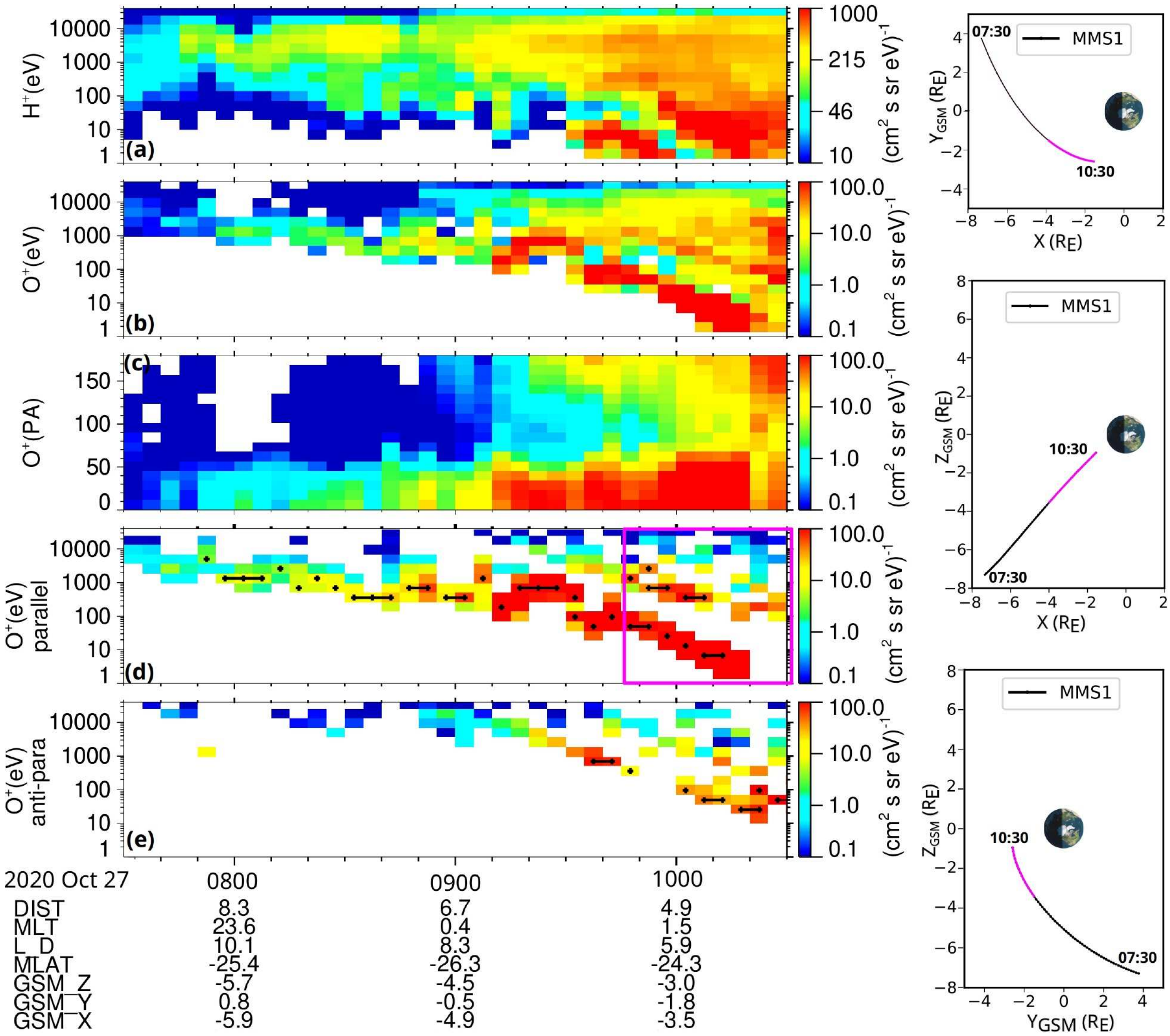

Figure 5. Observations of energetic streaming O^+ from the nightside auroral region. Panels from ton to down: Panel (a) is proton energy spectra over all angles. Panel (b) is O^+ energy spectra over all angles. Panel (c) is the pitch angle of O^+ at all energy. Panel (d) is the energy spectra of parallel O^+ with pitch angle between 0 and 60 degrees. Panel (e) is the energy spectra of antiparallel O^+ with pitch angle between 120 and 180 degrees. Black dots in panels (d, e) show the identified streaming O^+. MMS orbits are shown in projections of XY_{GSM}, XZ_{GSM} and YZ_{GSM} at the bottom of the figure.

continuously observes streaming O^+ until 10:10, as shown in Figure 5d. The energy of the observed streaming O^+ is high (>1 keV) at the start, and gradually decreases. At the end of the observation of the streaming O^+, around 10:10, the O^+ is as low as ~10 eV, and the satellite is less than 5 R_E from the Earth. Another dispersion of higher energy in the parallel direction is observed at the start of the pink box (09:45). Dispersions are also seen in the anti-parallel direction of different energies. The multiple dispersive streaming O^+ have been observed previously (Gkioulidou et al., 2019; Hull et al., 2019; Liu, Z.-Y., & Zong, Q.-G., 2022; Nosé et al., 2016, 2022; Sauvaud., 2004). They are likely to indicate contributions from direct injection from the northern and southern auroral ovals, and from injected O^+ that mirror in the opposite hemisphere. The dispersive pattern is both temporal and spatial. Ions from the same sources are separated by their velocity as the faster ions arrive at the location first and the slower ones later. The velocity filter effect separates the ions by their velocities. Slow ions are convected more inward during their time moving up the field line, and so end up closer to the Earth. The lowest energy outflowing O^+, as shown in the pink box and the pink segment in the orbit, is observed near the Earth. Later our statistical study will show the low energy streaming O^+ in the PS and PSBL are only observed near the Earth.

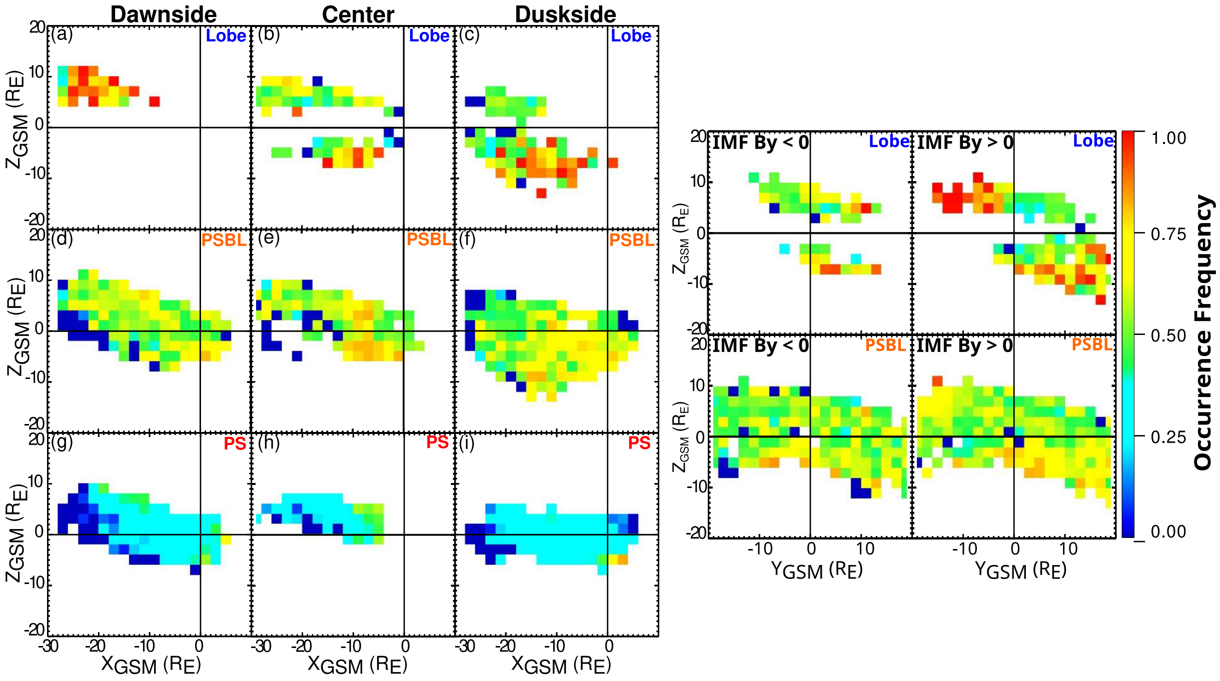

Figure 6. On the left are the occurrence frequency maps of streaming O^+ in the XZ_{GSM} plane, for different Y_{GSM} ranges (from left to right: dawn $-20\ R_E > Y_{GSM} > -5\ R_E$, center $-5\ R_E < Y_{GSM} < 5R_E$ and dusk $5\ R_E < Y_{GSM} < 20\ R_E$), and different regions (from top to down: lobe, plasma sheet boundary layer and plasma sheet). On the right are the Occurrence frequency maps of streaming O^+ in YZ_{GSM} plane, sorted by IMF B_Y (left column is for IMF $B_Y < 0$; right column is for IMF $B_Y > 0$), and regions (top: lobe; down: plasma sheet boundary layer). The color represents the occurrence frequency with dark blue as 0% and red as 100%. Correction factors for the compression have been applied.

4. Database of Streaming O^+

After running the identification program on MMS data from 2017 to 2020, we created a database including all the data observed within the magnetosphere (sheath and solar wind regions are excluded out with the same methods recorded in Liao et al. (2011)), with a flag indicating whether streaming O^+ is observed or not. The bidirectional streaming populations are also excluded, and only outflowing streaming O^+ is kept in the database so we can study the outflow and transport of the streaming O^+ population. For the time periods when either parallel or antiparallel streaming O^+ is observed, the properties of the streaming O^+ are recorded (energy, flux, and density) together with the magnetosphere dynamic conditions (storm phases, Dst, and Kp index). Dst and Kp Index and solar wind parameters are extracted from NASA/GSFC/s OMNI data set through OMNIWeb (King, & Papitashvili, 2020; Matzka et al., 2021; Nosé et al., 2015).

5. The Transport Paths

5.1. Occurrence Frequency

Occurrence frequency is defined as the number of streaming O^+ events divided by the number of total observations in a particular location and under certain conditions. Occurrence frequency shows the probability that the streaming O^+ will be observed in a specific region. The sites with high frequency represent the transport path of O^+ within the energy range of the instrument. By studying the occurrence frequency maps in different magnetospheric regions under various geomagnetic conditions, we investigate how O^+ ions are transported from the cusp and nightside auroral regions and enter the PS.

5.2. Occurrence Frequency Maps

Maps in Figure 6 are occurrence frequency maps of the streaming O^+, divided into different plasma regions (lobe, PSBL, and the PS) and locations, and/or sorted by different conditions. We divided the planes into a $2 \times 2\ R_E$ grid and calculated the occurrence frequency of the streaming O^+ in each bin. The color represents the occurrence frequency with dark blue as 0% and red as 100%. To make sure there are enough statistics for the maps, we require there to be more than 27 samples in each bin. The compression correction factor is applied.

The left group of maps in Figure 6 display the occurrence frequency of streaming O^+ in the XZ_{GSM} plane, for three ranges in Y_{GSM} (left to right: dawn, center, and dusk) and for different regions (top to down: lobe, PSBL, and PS). Overall, the streaming O^+ occurrence frequency decreases from the lobes, to the PSBL, to the PS. In Figures 6a–6c, both south and north lobes are clearly identified, although there is no data coverage in the south-dawn lobe. The occurrence frequency is above 80% in both north-dawn, south-center, and south-dusk, with the highest frequency near the Z_{GSM} around $+/-10\ R_E$. The high frequency regions are interpreted as the dominant transport path of the streaming O^+. The high frequency regions in Figures 6a–6c match the observations in Liao et al. (2010). There is a clear asymmetry in Figures 6b and 6c, with more frequent occurrence at south center and south dusk. This south-dusk preference of the streaming O^+ transport path is also discussed in Liao et al. (2010). The consistency of the lobe observation with the previous study provides good validation of our methods.

The occurrence frequency maps in the PSBL shown in Figures 6d–6f have higher frequency areas matching those in the lobe maps and a separate population at the near-Earth nightside region. On the duskside of the PSBL, as shown in Figure 6f, there is a high frequency region with occurrence frequency above ~70%, matching the transport path of streaming O^+ in the south dusk lobes, displaying straightforward evidence of the O^+ from the dayside cusp origin entering the PSBL. In the center PSBL, as shown in Figure 6e, the main part of the transport path is at the nightside around $X = -10\ R_E$ and Z_{GSM} between $-5\ R_E$ and $5\ R_E$, with occurrence frequency at ~80%. Part of the area overlaps with the streaming O^+ transport path in the southern lobe in Figure 6b. The rest does not have a matching area in the center lobes. One of the possibilities is that those ions are directly from the nightside auroral outflows. We will further discuss this population in the discussion section. On the dawnside of the PSBL, as shown in Figure 6d, the overall occurrence frequency is around 50%. There is a slightly higher rate region at the outer northern tail, matching the high frequency area in the dawnside lobe in Figure 6a, so this region could be the location where streaming O^+ enters the PSBL from the lobes. There are also high rates observed in the southern near-Earth region.

In the PS, the overall occurrence frequency of the streaming O^+ is the lowest (~27%), as shown in the last row on the left side of Figure 6. It indicates that O^+ streaming in the lobes, passing through PSBL, and entering the PS are scattered as they enter the high-density region, become isotropic, and can no longer be identified as a beam. The occurrence frequency is flat at most locations, indicating that the entry of streaming O^+ happens at all locations of PSBL. Some areas near the Earth reach a higher occurrence rate at ~50%. This near-Earth streaming O^+ is likely the low energy O^+ entry directly from the nightside auroral region into the PS.

5.3. Asymmetry of the Transport Paths Maps

Liao et al. (2010) discovered a similar asymmetry in the transport of the streaming O^+ from the cusp source and identified IMF By as the main driver of the asymmetry, along with the convection patterns at the source region. To compare the drivers of the asymmetric transport path observed by MMS in different regions with the Cluster results, we sort data into positive and negative IMF By and plot the lobe and PSBL occurrence frequency maps in YZ_{GSM} projection, as shown on the right side of Figure 6. When IMF By is positive, streaming O^+ travels preferentially at the north-dawn and south-dusk sides in the lobes and PSBL. When IMF By is negative, no noticeable asymmetry is observed. There is no asymmetry observed in the PS regardless of the direction of IMF By (not shown in this paper). This result agrees with the previous study of the transport path of O^+ steaming from the dayside cusp using Cluster data (Liao et al., 2010).

5.4. Transport Path of O^+ by Energy

The velocity filter effect separates the different energies of streaming ions. To better study energization and identify the sources of the streaming O^+, we plot the occurrence frequency maps and density maps of streaming O^+ in XY_{GSM} in different energy ranges and in different regions in Figure 7. Most of the data collected is for $|Z_{GSM}|$ less than $10\ R_E$. The arrangement of the maps is the same for different regions. The top two rows are for occurrence frequency and density maps in the lobe, the middle two rows are observations in the PSBL, and the bottom two rows are for the PS. Columns from left to right are for streaming O^+ with energy <100 eV, 100–1,000 eV, 1–3 keV, and >3 keV. The denominators (total number of observations in a bin) of the occurrence frequency are the same for all energy maps in the same region. The color bar for occurrence frequency is from 0 to

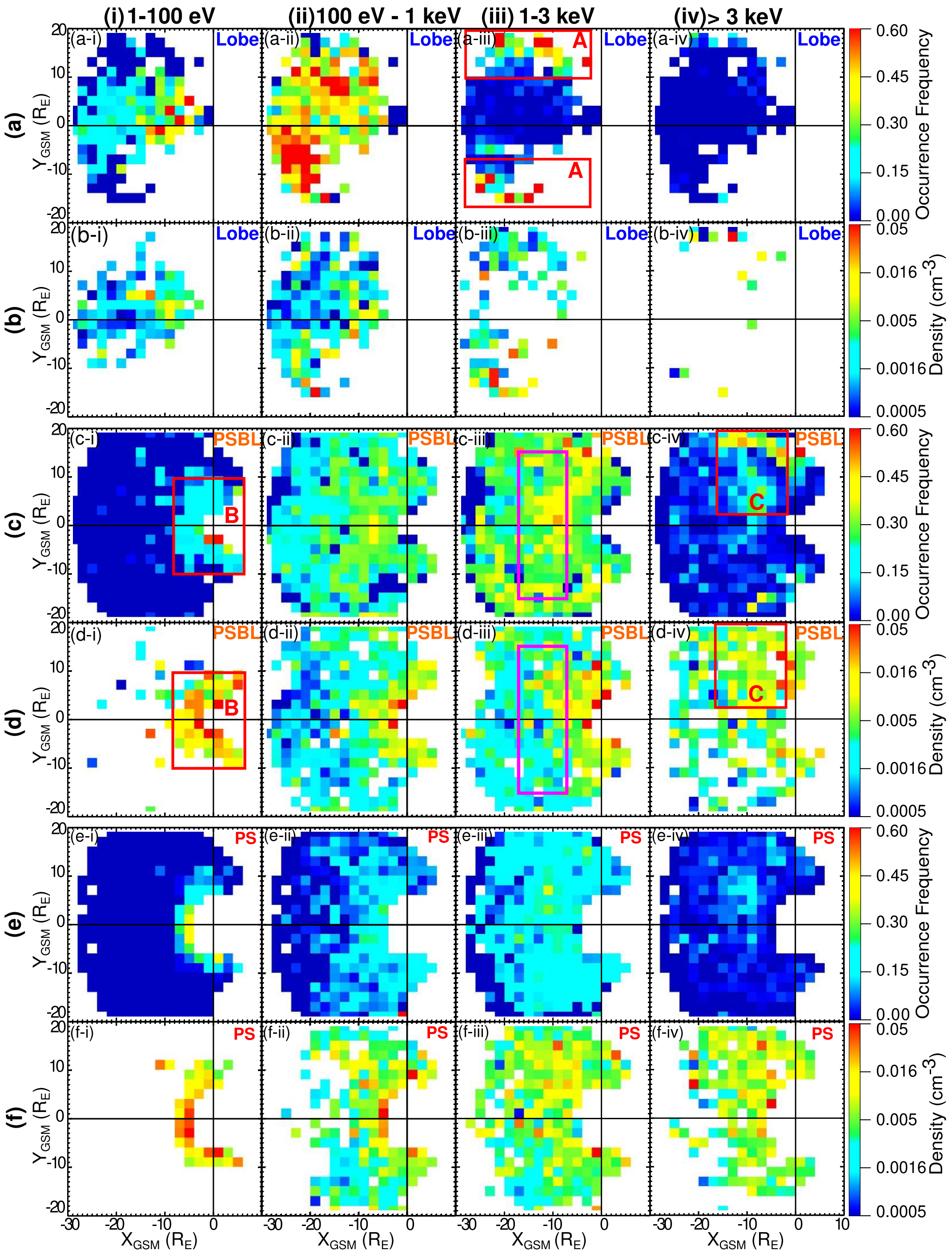

Figure 7. Occurrence frequency and density maps of streaming O^+ for different energy ranges (left to right: 1 eV–100 eV, 100 eV–1 keV, 1 keV–3 keV, > 3 keV) and in different regions (top to down: lobe, PSBL and plasma sheet). Correction factors for the compression are applied for the occurrence frequency maps. The color bar of the occurrence frequency is set from 0 to 0.6. The density color bar is set from 0.0005 to 0.05 cm^{-3}. Pink shapes are areas for fluence estimation in Section 7.

0.6 (0%–60%). The compression correction factor is applied. The density is calculated for all the observed streaming O^+ in each grid. The compression scheme has minimal effect on the density maps because the streaming O^+ is strongly anisotropic, and therefore concentrated in relatively few angular bins. The comparisons between density maps before and after compression are shown in Appendix A.

Rows a and b of Figure 7 display the occurrence frequency and density maps of streaming O^+ in the lobes. In panel (a–i), the streaming O^+ with low energy (1–100 eV) travels near the center of Y_{GSM} and can reach as far as $-28\ R_E$. It is possible that due to the variation of the convection field strength, which drives traveling distance of the outflowing O^+ in the lobe, the low energy lobe streaming O^+ can travel and arrive near the Earth under strong convection and reach further down the tail lobe when the convection field is weak. The density of this population, shown in panel (b–i), is slightly higher near the Earth and lower in the outer area, which may be due to the stronger outflow correlating with stronger convection during active times. The highest occurrence frequency in the lobes is observed in Figure 7a-ii, the map for streaming O^+ from 100 eV to 1 keV, with the highest rate on the dawnside close to the flank. The asymmetry is driven by the IMF By as discussed earlier. Figure 7a-iii shows that streaming O^+ from 1 to 3 keV are seen mostly near the dawn and dusk flanks. Panels (b–ii) and (b–iii) show that the number density of lobe streaming O^+ from 100 eV to 3 keV are similar ($\sim$0.002 cm^{-3}) to the number density in the lower energy range (1–100 eV). As discussed in the previous section, this dawnside lobe population is in the northern hemisphere and driven by positive IMF By. There are limited observations of streaming O^+ above 3 keV in Figure 7(a-iv), and they are mostly concentrated near the flanks as well.

Overall, in the lobes, streaming O^+ ions outflowing from the dayside spread across all HPCA energy ranges, with slower ions observed near the center of Y_{GSM} and faster ions traveling closer to the dawn and dusk flanks, as shown in area A in Figure 7(a-iii). Figure 4 shows an example of the energetic O^+ streaming in the outer direction. Noting that the Z_{GSM} coverage is within +/−10 R_E. There may be more energetic populations outside the satellite orbit. The density of cusp outflowing population is roughly from 0.001 to 0.005 cm^{-3} across energy ranges. Also, streaming O^+ lower than 1 eV, such as polar wind O^+, may also be missed due to the energy range of HPCA.

Row (c) and (d) show similar energy sorted occurrence frequency and density maps inside the PSBL. In panel (c–i), almost all low-energy streaming O^+ ions are near the Earth, with an occurrence frequency of ∼18%, as marked in area B. The transport path of the slow streaming O^+ in the PSBL, as shown in Figures 7c–7i, is quite different from the one in the lobes, as shown in Figures 7a–7i. Their density, shown in Figures 7d–7i area B, is around 0.02 cm^{-3}, which is much higher than the density of lobe streaming O^+ in Figures 7b–7i. The difference suggests that the observed low-energy outflowing O^+ in the PSBL are not from the lobes, that is, not originated from the dayside cusps. Their spatial distribution and observed regions are consistent with direct outflow from the nightside auroral. While this population is not clear in the occurrence frequency maps for higher energy O^+ in PSBL in Figures 7(c-ii and iii), we do observe a high-density ($\sim$0.01 cm^{-3}) population located at the similar near-Earth area in Figures 7(d-ii and iii). This is consistent with the event shown in Figure 5: streaming O^+ ions outflowing from the auroral oval cover a wide range of energies.

Streaming O^+ ions in the PSBL from 100 eV to 1 keV are observed over the whole region, with occurrence rates from ∼15% to ∼30% as shown in Figure 7(c-ii). Figure 7(d-ii) shows the density map for this population: the density is $\sim$0.002 cm^{-3} in most areas and there is a high-density region near the Earth. The similarity between the density range in outer area in Figure 7(d-ii) and the one of lobe streaming O^+ suggests that those PSBL streaming O^+ are coming from the lobe, with a dayside cusp source. The low-energy streaming O^+ in the lobes is likely accelerated during the entry into the PSBL and become more energetic and observed at higher energy range as streaming O^+ from 100 eV to 1 keV moving in the PSBL. This is consistent with the case study in Figure 3: the energy gradually increases when entering from the lobe into the PSBL. The high-density region near the Earth is at a similar location as those of low-energy PSBL streaming O^+ in Figures 7c–7i and d–7i, indicating that they are from the same nightside auroral source.

The highest PSBL occurrence frequency is observed in Figure 7(c-iii), the map of streaming O^+ from 1 to 3 keV. Because lobe streaming O^+ at this energy range are mostly found near the mantle area, the observed PSBL energetic streaming O^+ (1–3 keV) are most like from the combination of the entry of the lower-energy ions in the lobe, and direct outflow from the nightside auroral regions. O^+ ions streaming in the lobe are heated and accelerated as they enter the PSBL. The area of high occurrence rate (yellow) near the (−10 R_E, 0 R_E) in the PSBL maps for O^+ from 1 to 3 keV, as shown in Figure 7(c-iii), points out the location where auroral outflowing O^+ enters the PSBL directly along the closed field lines. The density of energetic streaming O^+ at 1–3 keV, as shown in Figure 7(d-iii), is overall higher than the less energetic O^+, supporting the population observed in Figure 7(d-iii) a highly mixed from both sources.

In Figure 7(c-iv), there are highly energetic (>3 keV) streaming O^+ observed at the duskside, as shown in area C. The duskside asymmetry may be due to the tilt of the orbits leading to a lack of data on the south-dawn side of the magnetosphere, which is evident in Figure 6. This duskside observation, as in Figure 7(d-iv) area C, has a density (~0.01 cm^{-3}) between the regular lobe entry O^+ (~0.002 cm^{-3}), and the auroral entry observed near the Earth (~0.02 cm^{-3}), which again suggests a mixed sources. Moreover, the near-Earth population that is evident in Figures 7d–7i and ii for streaming O^+ lower than 1 keV is not as clear in Figure 7(d-iii) and not seen in Figure 7(d-iv), indicating the more energetic streaming O^+ from the nightside auroral source can travel further out in the PSBL.

Overall, in the PSBL maps, we observed the streaming O^+ from the dayside cusps and the direct entry of nightside auroral outflow. Low energy O^+ from the lobes are accelerated during the entry and observed at higher energy inside the PSBL. Streaming O^+ from the nightside auroral sources are observed at all energies, with lower energy population closer to the Earth and more energetic O^+ observed further out.

For streaming O^+ inside the PS, the occurrence frequency (<20%) is lower than in the PSBL in general, as shown in row (e) in Figure 7, except for streaming O^+ lower than 100 eV. The decrease of occurrence frequency from the lobes to the PSBL and then PS is likely due to the streaming O^+ ions scattered and becoming more isotropic as they enter a denser region. The density of streaming O^+ in the PS averages around 0.005 cm^{-3}. As shown in Figures 7e–7i, streaming O^+ ions with low energies are found near the Earth, with similar location and density as the observation in the PSBL (but not seen in the lobe map). It displays where auroral outflowing O^+ streaming in the PSBL enter the PS, which can then feed the ring current. For streaming O^+ from 100 eV to 1 keV in the PS, as shown in Figure 7(e-ii), they are generally spread across the tail with an occurrence frequency of ~10%, except in the region that is far in the tail and center of the Y_{GSM} where the occurrence frequency is very low. The density pattern for PS streaming O^+ at the same energy range, as shown in Figure 7(f-ii), is similar to the PSBL density map. The missing population seems to be the low-density lobe entry population. One possible explanation is that because this region is where the magnetic field is more stretched and less dipole-like, ions are more likely to be scattered and less beam-like, and hence not detected as a streaming population. Another possibility is that those PSBL streaming population are accelerated and heated during entry, so they are not now categorized into higher energy maps. In Figure 7(e-iii), the occurrence frequency is flat at ~20% for streaming O^+ from 1 to 3 keV. In the corresponding density map in Figure 7(f-iii), there is a duskside preference, which is weak but exists in the PSBL density map in Figure 7(d-iii). For streaming O^+ above 3 keV inside the PS, the asymmetry in the occurrence frequency map (Figure 7(e-iv)) is probably inherited from the PSBL, consistent with streaming O^+ entering the PS from the PSBL, and partially due to the uneven orbit coverage of MMS.

6. Energy Maps

We further studied the energy distribution of the streaming O^+ to understand how outflowing O^+ with different energies behaves in the magnetosphere. We created median and minimum energy maps in different regions to assess how the energy profile changes during transport and entry into the PS. Figure 8 displays the median and minimum energy maps in XY_{GSM} for the lobe, PSBL, and PS. The number on each map gives the average value of the map. The line plots on the bottom are the median energy profile in the lobe along Y_{GSM} and minimum energy profile in PSBL along X_{GSM}.

6.1. Median Energy Maps

The median energy is lowest in the lobe (averaged at 591 eV), higher in PSBL (averaged at 1,409 eV), and highest in PS (averaged at 1,750 eV). Within the lobes, the median energy increases gradually as $|Y_{GSM}|$ increases, that is, low-energy O^+ is observed in the center while energetic ions are observed further out in the $|Y_{GSM}|$ direction. The pattern is confirmed by the line plot at the bottom of Figure 8, where high energies are most likely to be observed at large Y_{GSM}. While the velocity filter effect probably plays a key role in this pattern, this energy pattern indicates limited energy dependence of streaming O^+ on X_{GSM}.

In the PSBL, a weak radial dependence is observed, with the lowest energy (~100 eV) observed on nightside near the Earth, and the highest observed further down the tail (~300 eV–~3 keV). There is a slight tendency for the highest energy O^+ to be observed near the flank area (large $|Y_{GSM}|$), and an asymmetry with more energetic O^+ observed on the duskside of the PSBL. The line plot on the bottom right of Figure 8 confirms that the low energy O^+ are only observed fairly close to the Earth. Comparing with the maps in the row (e) of Figure 7, the near-Earth population with energy lower than 300 eV are the streaming O^+ from the nightside auroral oval while the more

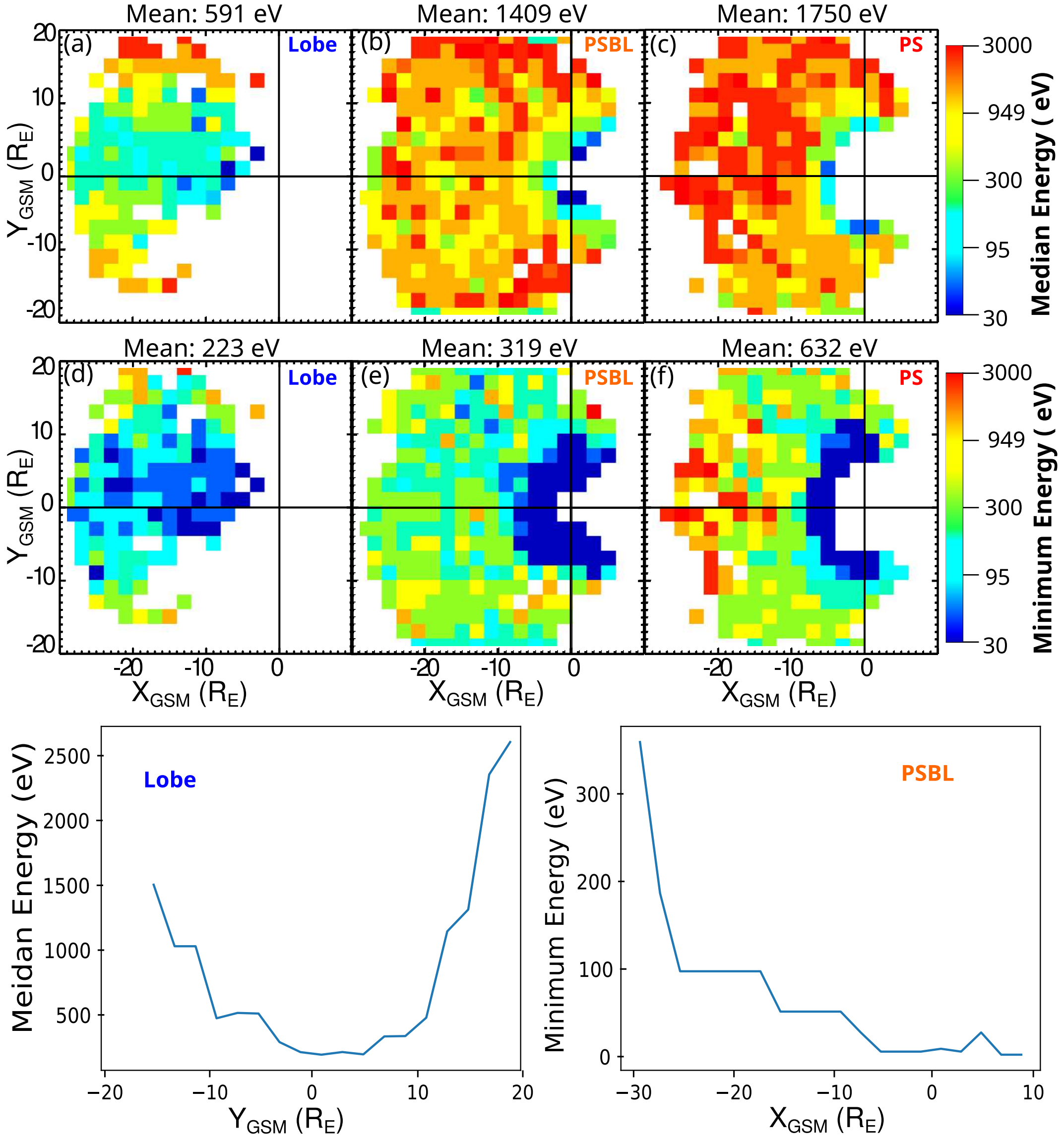

Figure 8. Median (top row) and minimum (bottom row) energy maps of streaming O^+ in XY_{GSM} projections in different regions (left to right: lobe, plasma sheet boundary layer and plasma sheet). The numbers on maps show the average value of the maps. The line plots on the bottom are the median energy profile in the lobe along Y_{GSM} and minimum energy profile in PSBL along X_{GSM}.

energetic population at outer area are populations mixed from the accelerated O^+ from the lobe and energic part of auroral outflows.

Inside the PS, the averaged energy is the highest among all three regions. We still observe low-energy O^+ streaming near the Earth but with greater energy than those observed in the PSBL. In most parts of the PS, the energy is greater than 1 keV. Again, the low-energy population is likely to be from the nightside auroral region while the energetic population is from mixed sources. There is an asymmetry with higher energy ions observed on the duskside, which is consistent with the observation in Figures 7(c-iv) and (f-iv).

6.2. Minimum Energy Maps

The 2nd row Figure 8 plots the minimum energy maps of streaming O^+ in the XY_{GSM} plane. Each grid point shows the lowest energy of all the identified streaming O^+ events at each location. The minimum energy map shows where the low-energy O^+ cannot reach.

Like the median energy maps, the minimum energy generally increases with plasma beta. In the lobes, the minimum energy is the lowest at the center of Y_{GSM} and increases gradually toward the flanks. Most of the low energy O^+ (<30 eV) are constrained near the Earth and do not make it far down to the tail, as expected for the velocity filter effect. Streaming O^+ less than 80 eV mostly streaming near the center of Y_{GSM}, does not reach area with the large Y_{GSM}.

As in the median energy map in the PSBL, two distinct populations are observed in the PSBL minimum energy maps: the population with low energy (<30 eV) and only observed near the Earth, and the population further out, with minimum energy range around 300 eV. It is consistent with velocity filter effect that slow outflowing ions reach the PS closer to the Earth not further down the tail.

A similar trend is observed in the PS. The streaming O^+ ions with the lowest energy are only observed near the Earth, and the minimum energy of streaming O^+ in the outer areas are much higher. The overall energy is higher in the PS than the observed ones in the PSBL, implying either acceleration occurred during O^+ entry from the PSBL into the PS, and/or less energetic streaming O^+ ions are easier to be scattered and lose their streaming features when they enter the PS.

At the center of Y_{GSM} and $X < -10\ R_E$, there is an area where the lowest energy observed is above 700 eV. This is consistent with Figure 7(c-ii): the streaming O^+ lower than 1 keV is not observed in the center in Y_{GSM}. By comparing this with Figure 7(c-ii), one can see that this increase in minimum energy is due to the lack of low energy population in this area. The more stretched magnetic field in this area that efficiently in scattering the streaming population may be the cause of this.

7. The Impact of Geomagnetic Activity

Because the data collection time covers the end of the declining phase of solar cycle 24, there are only a few magnetic storms during 2017–2020 and the F10.7 is below 100 sfu (10^{-22} W m^{-2} Hz^{-1}) the whole time.

As a result, we have limited storm time data to study the storm phase impact on the maps of streaming O^+, and so we use the more general Kp index to study activity dependence. To investigate how the geomagnetic activity influences the transport and the entry, we plot, in Figure 9, the streaming O^+ maps in occurrence frequency, density, median and minimum energy, sorted into two Kp ranges: Kp < 2 and Kp > = 2, in different regions.

Inside the lobe (the two left columns in Figure 9), the occurrence frequency, density, median and minimum energy increase when KP index is higher. This increase is likely due to a more frequent, stronger and more energetic O^+ outflows from the dayside cusp source during the active time and higher convection brings energetic O^+ closer to the Earth. The location of the lobe is also different for different Kp intensity. During more active times, the lobe has a wider coverage in Y_{GSM} direction, especially on the duskside. The different topology is consistent with a thinner active time PS.

The middle two columns in Figure 9 display the Kp index impact on the PSBL streaming O^+. When Kp index is higher, the occurrence rate is clearly higher for both the near-Earth population and the O^+ entering at larger distance. Similar increases can be seen in the density map, indicating a more intense O^+ population in the PSBL during non-quiet time. There are also increases in the median energy maps, which may be the result of a stronger acceleration or a shift on the energy distribution of the outflowing O^+ when Kp index is higher. The increase in the minimum energy map is evident but not as strong, which may be because it is the minimum convection that drives the minimum energy maps. The streaming O^+ from the auroral sources, identified as the low-energy high-density population observed at the inner-edge of the PS, is clearly enhanced and more energetic during active times. Because the O^+ from the dayside cusp source is mixed with energetic O^+ from the auroral sources at the larger distance, there is no direct evidence for the enhancement of lobe source O^+ in the PSBL. However, it is expected that due to the stronger outflow, the more dynamic magnetosphere is likely to bring more lobe O^+ into the PSBL.

The right two columns in Figure 9 show how streaming O^+ inside the PS changes for different Kp ranges. When KP is higher, the streaming O^+ ions in the PS are more frequently observed, and their density is also higher, showing a stronger and more frequent input of streaming O^+ into the PS, forming a more populated PS. The increase in the PS median energy map shows the O^+ entering the PS is more energetic when the magnetosphere is more active. There is a slight increase in the minimum energy map.

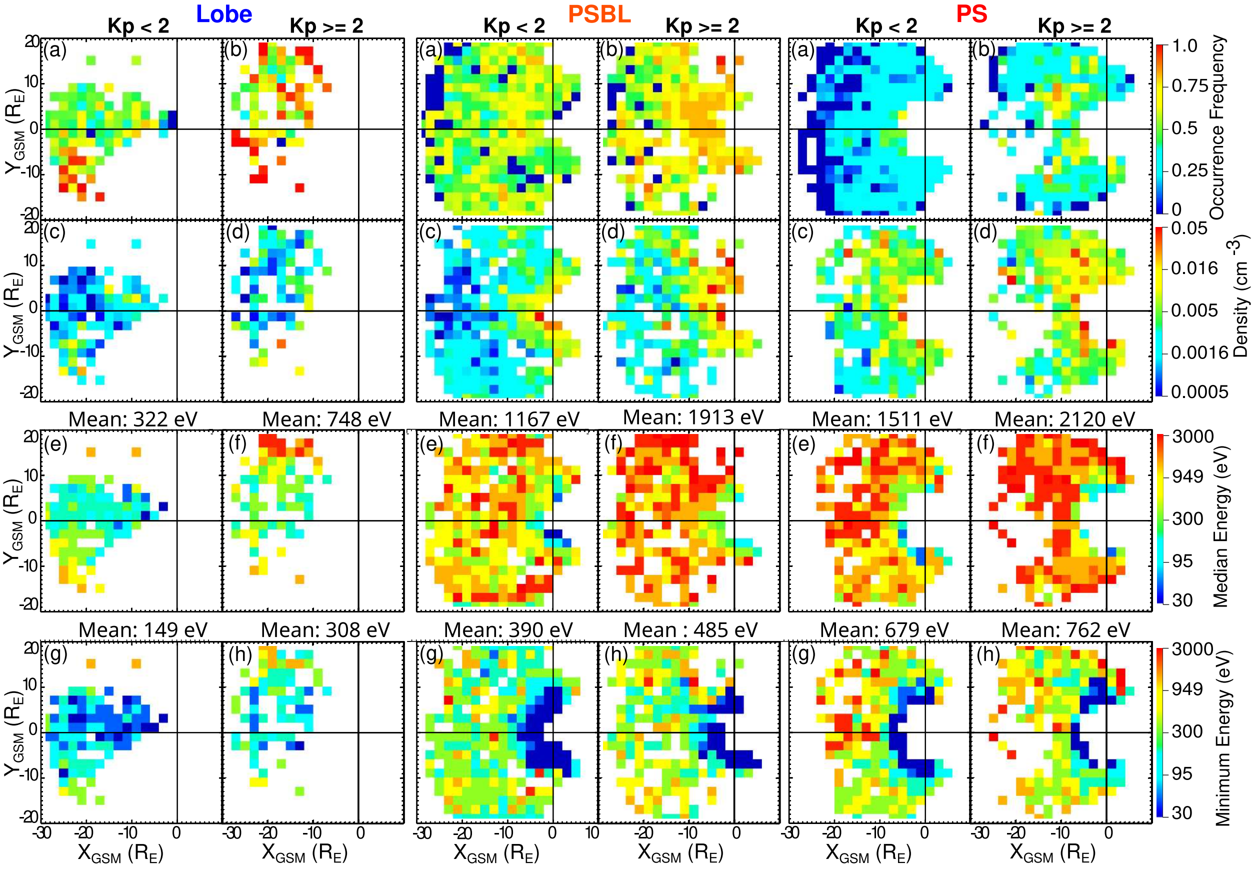

Figure 9. Maps of, from top to down, occurrence frequency, median density, median energy, and minimum energy, divided into different regions (lobe, plasma sheet boundary layer and plasma sheet), and sorted by KP index (for each region, left column: KP >= 2, right column: KP < 2). Correction factors for the compression have been applied to the occurrence frequency maps. The number on energy maps is the average value of the map.

Figure 9 showed how streaming O^+ in different regions reacts to a more active magnetosphere. It confirms that higher activity correlates with more frequent and stronger O^+ outflow from the dayside cusp and night auroral region, leading to a more frequent, stronger and more energetic O^+ input into the PS, which can lead to a stronger ring current during storms.

8. Discussion

8.1. Streaming O^+ Origin and Transport Path

The occurrence frequency and density maps in Figure 7, and the energy maps in Figure 8 present the distribution of the streaming O^+ in the magnetosphere and their density and energy profiles. As discussed earlier, there are three distinct populations.

The streaming O^+ ions from the dayside cusps are traveling in the lobes with a wide energy range (<3 keV) and location extent. The spatial distributions show an energy dependence on Y_{GSM}: slower O^+ ions traveling in the center of Y_{GSM} and more energetic ions traveling near the larger Y_{GSM}. Seki et al. (2000) have previously reported similar streaming O^+ with high energy observed in the lobe/mantle area with large $Y_{GSM.}$ The energetic O^+ above 3 keV may reach the flanks outside $Y_{GSM} = 20\ R_E$, and leak into the magnetosheath. Their transport path has an IMF By driven asymmetry that preferentially travels on the north-dawn and south-dusk sectors. The energy pattern of streaming O^+ in the lobes with gradient dependence on Y_{GSM} and limited dependence on X_{GSM} is likely to be the average outcome of convection driven velocity filter effect. Seki et al. (2000, 2002) have previously reported similar streaming O^+ with high energy observed in the lobe/mantle area with large $Y_{GSM.}$ They suggested that the dayside equatorially trapped O^+ entering an open flux tube after possible energization at the reconnection site and mirror reflection near the cusp could be the source of those energetic streaming O^+ observed

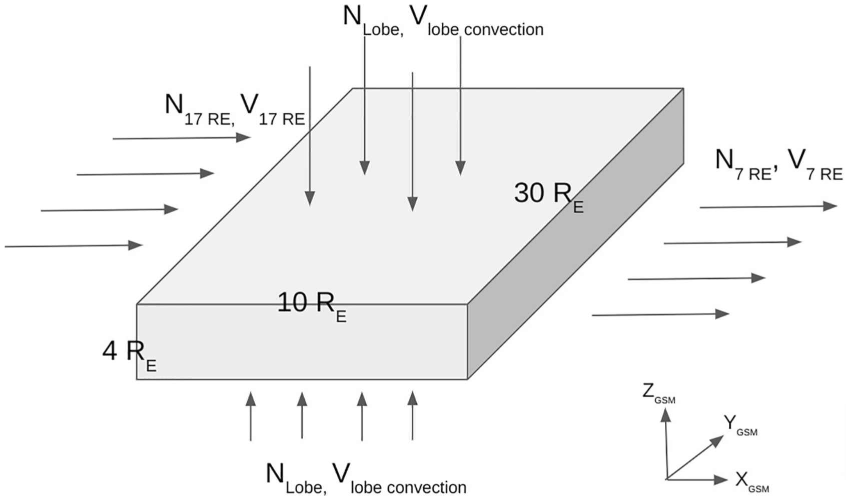

Figure 10. Schematic graph showing the slab model of plasma sheet with ions streaming in from magnetotail, lobes and out from the plasma sheet. The dimensions are X: [−7 R_E, −17 R_E], Y: [−15 R_E, 15 R_E], Z: [−2 R_E, 2 R_E].

near the flank region. Arvelius et al. (2005) observed keV level O^+ inside the high-altitude polar cap (6–12 R_E), suggesting that ionospheric O^+ ions can be accelerated and/or heated in the polar cap above 8 R_E. The streaming O^+ inside the lobes can enter the PSBL at all locations with acceleration that brings all of them above 100 eV. The energy pattern is, however, lost once the population enters the PSBL. The streaming O^+ has an average density of ~0.002 cm^{-3} in the lobes, and the density increases in the PSBL, and becomes even higher as they enter the PS. This population becomes more frequent, more intense and more energetic when the magnetosphere becomes more active.

Streaming O^+ ions close to the Earth are observed in the PSBL, and then convect into the PS. Their median energy is very low (~30 eV), but the energy range extends to the keV range (<3 keV). The median density is high, above 0.02 cm^{-3}, inside the PSBL and PS. Most of them are to be from the nightside auroral region, with some low-energy population from the polar wind. The auroral source, even if mostly at low energy <100 eV is not limited to low energies. The low threshold of HPCA detectable energy is 1 eV, so O^+ ions with energy below 1 eV cannot be detected. The undetected O^+ population at low geocentric distance are likely to be at very low energy and would require extra acceleration to reach a high enough energy to contribute to the hot PS.

There is a third high-energy and high-density population observed at the south-dusk side of the PSBL and the PS. It is the main contribution to streaming O^+ above 3 keV inside the PSBL and the PS. It is different from the lobe entry population due to its high density and much higher energy. The dusk preference of this population may be due to the asymmetry of the MMS orbits that lead to a limited coverage at south-dawn section. The median density of this population (~0.01 cm^{-3}) is between the typical lobe density (~0.002 cm^{-3}) and the density of the near-Earth dense population (~0.02 cm^{-3}), suggesting this population may be a mixture of streaming O^+ from different sources. It likely contains the energetic portion of the nightside auroral outflows, which are from the same source as the inner edge low-energy high-density population but travel further down the tail due to the energy of the ions, as shown in Figure 1.

8.2. The Contribution of Streaming O^+ to the Plasma Sheet Population

To investigate how the streaming O^+ from various sources impacts the composition of the near-Earth PS from 6 to 15 R_E, we need to estimate the entry and loss of ions inside the PS. As a first-order approach we make a simplifying assumption that the PS is a rectangular slab, as shown in Figure 10, with *X* between (−7 R_E, −17 R_E), *Y* between (−15 R_E, 15 R_E), and *Z* between (−2 R_E, 2 R_E) and that for "average" (mainly quiet) times, there is a steady state, so that the inflow should equal the outflow. We then examine the inputs and the outputs of the PS to study the contributions of various sources. The choices of 7 and 17 R_E are based on data availability from the literature and our study. We assume the net flow in the cross-tail direction is zero, that is, the same number of ions drifting in from the dawnside are drifting out on the dusk side. We note that the extracted values are based on

Table 1
Data for Estimation of Plasma Sheet ion Composition

Ion specie	F10.7	Flow type	Measurement	Reference	Occurrence rate
H^+ Density (cm^{-3})	>100	Lobe input	0.14 (0.06–0.24)	Engwall et al. (2008)	68%
	All	Tail input	0.27 (0.21–0.32)	Maggiolo and Kistler (2014)	–
	All	Auroral input	Unknown	–	–
	All	Output	0.86 (0.82–0.92)	Maggiolo and Kistler (2014)	–
O^+ Density (cm^{-3})	<100	Lobe input	0.0019 (0.0008–0.0057)	This study	63% (50%–76%)
		Tail input	0.005 (0.005–0.005)	Maggiolo and Kistler (2014)	–
		Lobe input + Auroral input (PSBL observation)	0.0028 (0.0014–0.0063)	This study	60% (53%–68%)
		Output	0.064 (0.05–0.078)	Maggiolo and Kistler (2014)	–
	>100	Lobe input	0.009 (0.004–0.023)	Liao et al. (2011) (majority > 100)	66%
		Tail input	0.011 (0.003–0.028)	Maggiolo and Kistler (2014)	–
		Auroral input	Unknown	–	–
		Output	0.17 (0.14–0.19)	Maggiolo and Kistler (2014)	–
Convection velocity (km/s)	<100	Lobe input	40.0 (33.7–56.0)	This study	–
	All	Tail input	21.3 (19.8–24.7)	Chong et al. (2021)	–
		Output	11.5 (8.85–16.7)	Chong et al. (2021)	–
	<100	PSBL observation	38.9 (33.4–46.1)	This study	–

Note. Data includes median values and variances, that are extracted and aggregated from references and data from this statistical study with MMS/HPCA data.

average values, so the estimation is for quiet time. During active times, the density and convection velocity are expected to be higher.

There are three known sources that contribute to the main composition of the PS from 7 to 17 R_E: the streaming ions entering from the north and south lobes, the streaming ions enter from the nightside auroral region, and the more distant PS convecting Earthward at 17 R_E. The loss, or output from the PS is the Earthward convection of ions at 7 R_E into the inner magnetosphere. To estimate the input and output of the PS, we need to calculate the fluence, the number of ions per second flowing through an area. The fluence is the product of the number flux and the size of the area, and the number flux can be calculated by multiplying the plasma density and the convection velocity. To estimate the fluence of H^+ and O^+ from the lobes and PSBL we sum up the products of the ion density (in each grid) and its occurrence frequency, and multiply summed-up result by the convection velocity and the area of both north and south lobes ($10 \times 30\ R_E \times 2$). The input from the tail PS is the product of ion density at 17 R_E PS, the inward convection velocity at 17 R_E and the area of the cross-section of the PS ($30 \times 4\ R_E$), as shown in Figure 10. The output to the inner magnetosphere is calculated by multiplying the PS ion density at 7 R_E by the inward convection velocity at 7 R_E and the cross-section of the plasma sheet, $30 \times 4\ R_E$.

We extracted density and convection velocity data from a number of studies (Chong et al., 2021; Engwall et al., 2009; Liao., 2011; Maggiolo & Kistler et al., 2014) and cross checked the number with others (Angelopoulos et al., 1993; Chen et al., 2007; Haaland et al., 2008; Juusola, Østgaard, Tanskanen, Partamies, & Snekvik, 2011; Juusola et al., 2011b; Kistler & Mouikis, 2016; Miyashita et al., 2020; Mouikis et al., 2010). Table 1 shows the extracted and aggregated data and the references they were extracted from. The density and occurrence frequency in the lobes and PSBL are extracted from the data from this study. The convection velocities in the PSBL and lobes are calculated from the perpendicular velocity of proton, measured by MMS/HPCA. The result of the fluence estimation is shown in Table 2.

As the O^+ from both dayside and nightside sources are mixed inside the PSBL, to estimate the fluence of O^+ from the nightside auroral outflows, we can calculate the total fluence of streaming O^+ observed in the PSBL and subtract the lobe fluence from it. We use the same area as the lobe entry: $10 \times 30\ R_E$ for streaming O^+ coming from northern and southern hemispheres. The PSBL fluence is then the product of PSBL density, velocity perpendicular to the entry surface and the areas. The median values and variances are shown in Table 1 and the

Table 2
The Estimation Results of the Slab Model

Ion species	F10.7	Lobe input [10^24/s]	Tail input [10^24/s]	PSBL Observations[10^24/s]	Total input [10^24/s]	Output [10^24/s]
H^+	All	17.5 [6.96, 32.2]	29.2 [18.6, 42.0]	Unknown	46.7 [25.6, 74.2]	54.8 [29.8, 83.5]
O^+	<100	1.95 [0.59, 9.99]	0.53 [0.49, 0.61]	2.17 [0.76, 6.16]	2.7 [1.25, 6.78]	3.57 [2.16, 6.33]
	>100	5.78 [2.17, 20.7]	1.14 [0.29, 3.37]	Unknown	6.92 [2.46, 24.1]	9.26 [6.08, 15.7]

Note. The results are calculated using the data from Table 1. The sum of inputs is the total fluence of lobe input, tail input and auroral input. Values in the bracket show the quartiles of the value.

calculated fluences can be found in Table 2. As mentioned earlier, data used in this study is collected when F10.7 is below 100 sfu.

Table 2 shows the estimated fluence of input of the lobe, entry from the more distant magnetotail, PSBL observation, and the loss into the inner magnetosphere. The PSBL observation contains both lobe entry and auroral outflows. Cully et al. (2003) showed that the fluence of O^+ outflow correlates strongly with F10.7, which is not true for H^+. The fluence of O^+ net outflow is ∼10 times higher above 125 sfu than below 125 sfu. Thus, the fluence calculation of O^+ is done for F10.7 above and below 100 sfu. The total fluence of H^+ input from the lobe ($1.75 \times 10^{25}\ s^{-1}$) and magnetotail ($2.92 \times 10^{25}\ s^{-1}$) accounts for ∼85% of the total ion fluence ($5.48 \times 10^{25}\ s^{-1}$) into the inner magnetosphere. Although the error bar is large because the data is collected from references using long-term data, it clearly supports that H^+ from the lobes and the more distant magnetotail, are the dominant sources for PS H^+. The auroral outflows may contribute but are not likely to be substantial. Nowrouzi et al. (2023) shows that the H^+ outflow is on the same order as the O^+ outflow, implying that the fluence of the auroral outflowing H^+ is on the order of $10^{23}\ s^{-1}$, much lower than the other sources. The estimated fluence of lobe H^+ has an energy range from 1 to 60 eV. They may be directly from the polar wind or outflowing from the dayside cusp.

For O^+, the dayside cusp source is more important. When F10.7 is low, the total fluence of O^+ from the lobe ($1.95 \times 10^{24}\ s^{-1}$) accounts for ∼55% of the O^+ that convects towards the inner magnetosphere. The observed PSBL fluence ($2.17 \times 10^{24}\ s^{-1}$) is similar to the lobe observations. The auroral outflow is likely to be a minor source ($\sim 2.2 \times 10^{23}\ s^{-1}$) of O^+ in the hot near-Earth PS during quiet-time. The total of all the known inputs is at $2.7 \times 10^{24}\ s^{-1}$, which is smaller but within the same order as the output at 3.57×10^{24}/s, considering the variance. The low energy O^+ ($1.7 \times 10^{23}\ s^{-1}$, estimation not shown in the paper) from the nightside auroral region reaches the equatorial region close in, and thus it cannot contribute to the hot PS beyond 7 R_E, but may directly drift to the inner magnetosphere.

When F10.7 is above 100, we do not have data for estimation for O^+ from the auroral region. We can then determine the importance of the nightside auroral outflow contribution by comparing the ion entry from the magnetotail and the lobes to the ion loss near the Earth. The influence of lobe ($5.78 \times 10^{24}\ s^{-1}$) makes up ∼62% of the output fluence ($9.26 \times 10^{24}\ s^{-1}$) of O^+ to the inner magnetosphere, which is even higher than the same contribution (55%) for low F10.7. The result implies that, during quiet times, O^+ from the dayside cusp provides a significant fraction of the PS O^+ at 7 R_E, regardless of EUV levels, and when F10.7 is higher, the cusp outflowing O^+ has an even stronger contribution.

It is important to point out again that the estimations here are based on the median values, which are dominated by quiet and the non-storm time condition. In Section 6, we showed that during active times the occurrence frequency and density are higher, and energy patterns are different, all leading to an increase in the fluence and different energy profile of inflow ions. The contribution of storm time O^+ could also be quite different, due to a much-enhanced dayside cusp outflow and a much more dynamic magnetosphere. Kistler et al. (2010) shows that during storm time, the density of lobe beams can reach as high as 0.1 cm^{-3}, more than 10 times the quiet time value. Hence, it is likely that cusp origin O^+ is also the major contribution of the O^+ in the hot PS during storm time and, at this moment we do not have enough data to make a good estimation of inflow and outflow of active time hot PS. But this paper has clearly shown the importance of the cusp source during average times.

9. Conclusion

We investigated the contribution of the O^+ from different sources as they are entering the PS. The IMF By driven asymmetry of cusp origin O^+ observed in the lobe is consistent with the previous study. The energy pattern of lobe O^+ has a strong Y_{GSM} dependence, with low-energy O^+ streaming closer to the tail center and high energy (1–3 keV) O^+ streaming near the flanks. O^+ from the nightside auroral oval are observed in the PSBL/PS mixed with the lobe incoming population. We were able to distinguish part of this source: the low energy (<100 eV) O^+ near the Earth with high-density (>0.02 cm-3), and the energetic (>3 keV) streaming O+ with similar density (~0.01 cm^{-3}) out on the duskside of the PSBL/PS.

To study the sources of the PS ion composition quantitatively, we estimated the contributions of the different sources to the flow of H^+ and O^+ ions through the PS between 7 and 17 RE with a slab model, using the observations from this study and the data extracted from previous studies. The estimation result indicates that during quiet times, the PS H+ near the Earth has a mixed source of the dayside cusps, the polar wind and Earthward convection from the distant tail, with the last one contributing most. The O^+ in the same region are also from various sources, with the dayside cusp likely providing the highest contribution.

Appendix A: Impact of Compression Scheme

The onboard "lossy" compression scheme employed by HPCA on MMS drops the least significant bit in any accumulated energy-angle-angle bin for each species before downlinking the data to the ground (Young et al., 2016). Therefore, in Fast and Survey modes, for each 16 energy—8 azimuth-angle—8 elevation-angle matrix accumulated over a ½ spin, any bins with single counts are eliminated. This can result in significantly lower fluxes for the minor species and/or low energy populations, where single counts in each energy-angle-angle bin are commonly observed. It should be emphasized that the impact is greater for isotropic populations at all energies where counts are equally spread over all angular bins, compared to anisotropic populations for the same total number of counts where the counts are concentrated in a smaller number of angular bins. In Burst mode the energy-angle-angle resolution is higher (64 energy—16 azimuth-angle—16 elevation-angle). Therefore, for each bin in a Fast/Survey mode matrix there are 16 corresponding bins in Burst mode and therefore counts will be spread over 16 bins instead. In Burst mode the impact of the compression is even greater since the counts in one survey mode energy-angle-angle bin are spread over 16 bins, resulting in a much higher probability that single counts will be dropped. The "lossy" compression operated continuously from the beginning of the mission. It was temporarily turned off under Fast Survey mode from 2018-05-27 to 2018-09-25 and for the entire 2019 tail season from 2019-04-16 to 2019-08-17. The lossy scheme was permanently turned off after 2022-05-24. To analyze the impact of the "lossy" compression scheme on the occurrence frequency maps that we constructed for this study and to adequately correct those, we simulated the "lossy" compression algorithm effect on the energy-angle-angle data and applied it to the data from a period when the compression scheme was turned off during the tail seasons of 2018 and 2019: Fast Survey mode from 2018-05-27 to 2018-09-25, and 2019-04-16 to 2019-08-17. This gives us the ability to derive empirical occurrence frequency correction factors that we can apply to the compressed data.

By comparing the occurrence frequency maps with and without the compression for the same period, we calculated empirical occurrence frequency correction factors as a function of the "compressed" occurrence frequency. Figure A1 panels (a, d, and g) shows the original maps from periods when the "lossy" compression is turned off, panels (b, e, and h) show the maps from the same periods after simulated compression is applied, and panels (c, f, and i) show the simulated compression maps corrected using our empirical correction factors. The "Compressed" panels show that the occurrence frequency of the streaming O^+ is clearly reduced after the compression is applied. After applying the correction factors, the "Corrected" panels show that the overall occurrence frequency goes back to the original level and the patterns of the occurrence frequency map are restored in all regions.

Figure A2 shows the correction factor depending on the occurrence frequency, sorted by different regions (the lobes, PSBL, and the PS). As expected, the correction factors are above one, which means the occurrence frequency with the compressed data is much lower than the actual value, and the loss is more significant for lower occurrence frequency. To compensate for the loss, for all the occurrence frequency maps presented in this paper, we apply the piecewise-linear factors shown by the black lines in Figure A2 as a correction to bring the occurrence

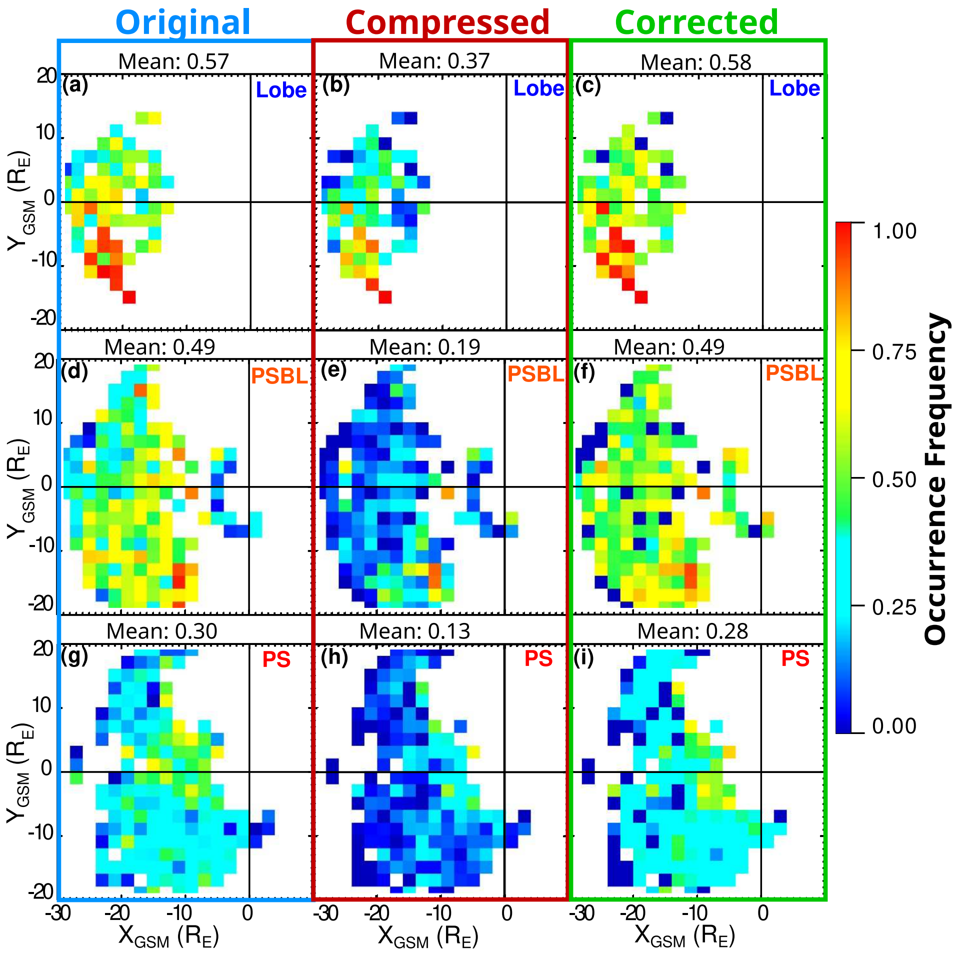

Figure A1. Occurrence frequency maps without "lossy" compression (1st column), with (2nd column) simulated compression, and (3rd column) with correction factors applied on the compressed data. Rows from left to right show the maps from the lobes, the PSBL, and the PS. The data shown were collected during times that compression scheme was not used during 2018–2019. The number in each plot shows the average occurrence frequency.

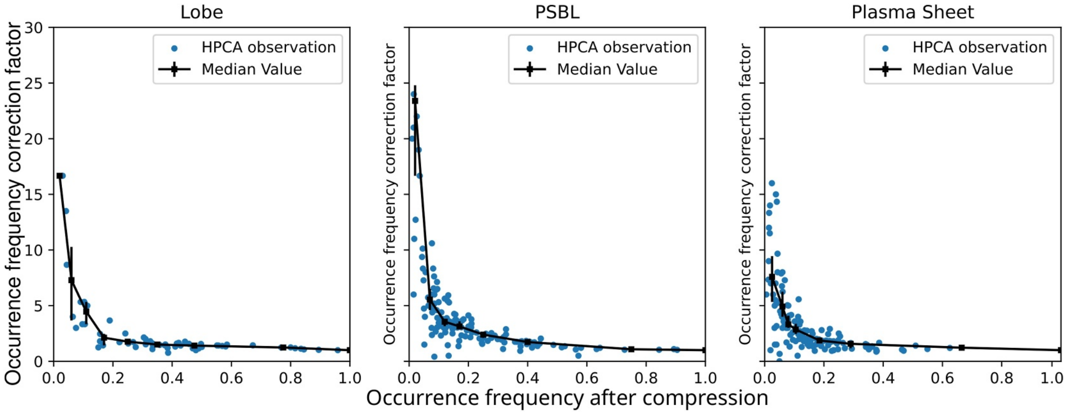

Figure A2. Dependence of the Occurrence frequency compression correction factor on the occurrence frequency observed after compression, for different regions.

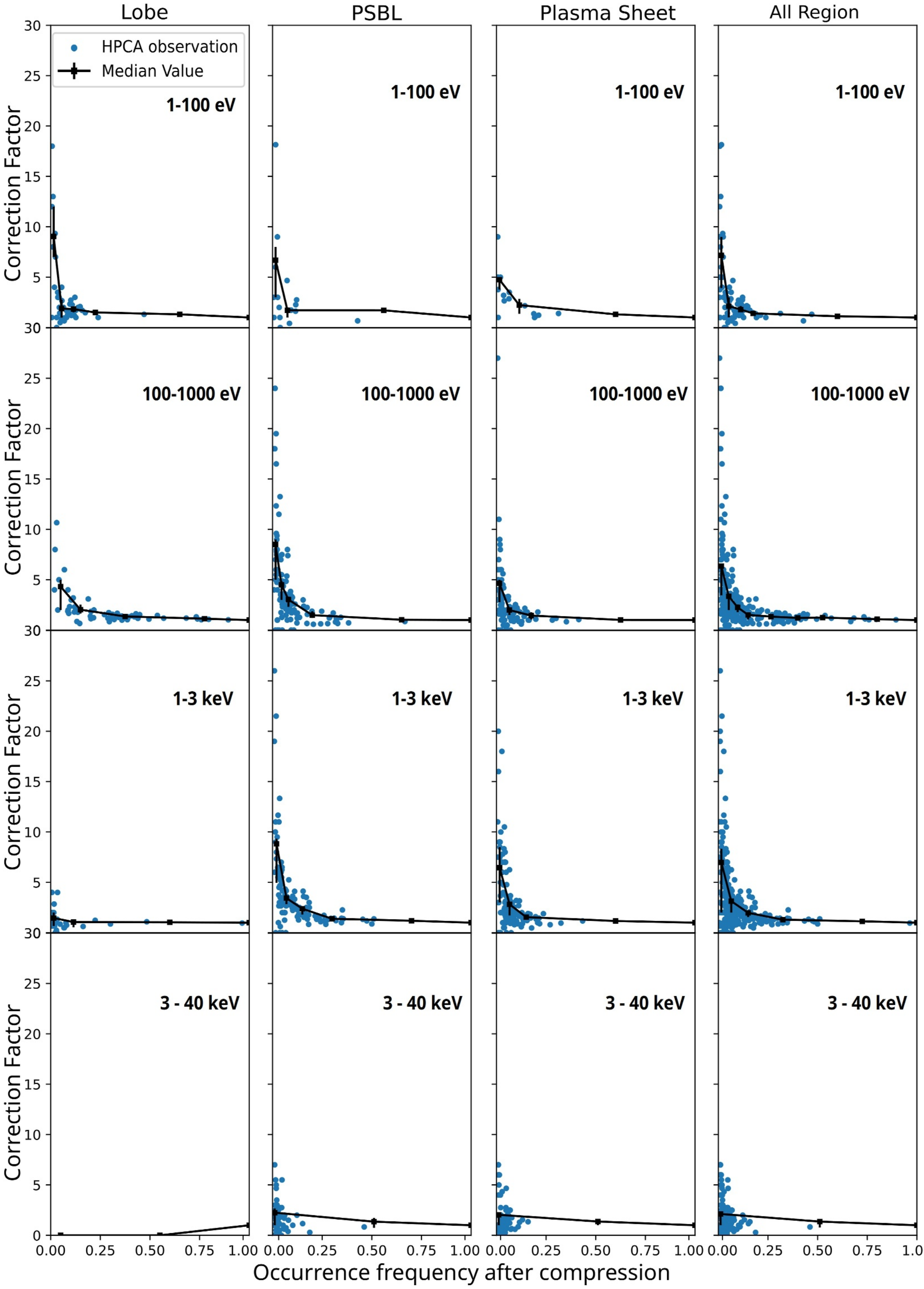

Figure A3. Dependence of the Occurrence frequency compression correction factor on the occurrence frequency observed after compression, sorted by energy range (rows) 1–100 eV, 100–1,000 eV, 1–3 keV and > 3 keV, and by different regions (columns). Blue dots are the observations, and the black lines show the median value and quartile of the data.

frequency closer to the true value. The correction factors here are applied to all the occurrence frequency maps in the paper except Figure 7, which applies the energy-depending correction factors in Figure A3. Taking into account the effect that the "lossy" compression scheme has for the different energies as well (an electrostatic

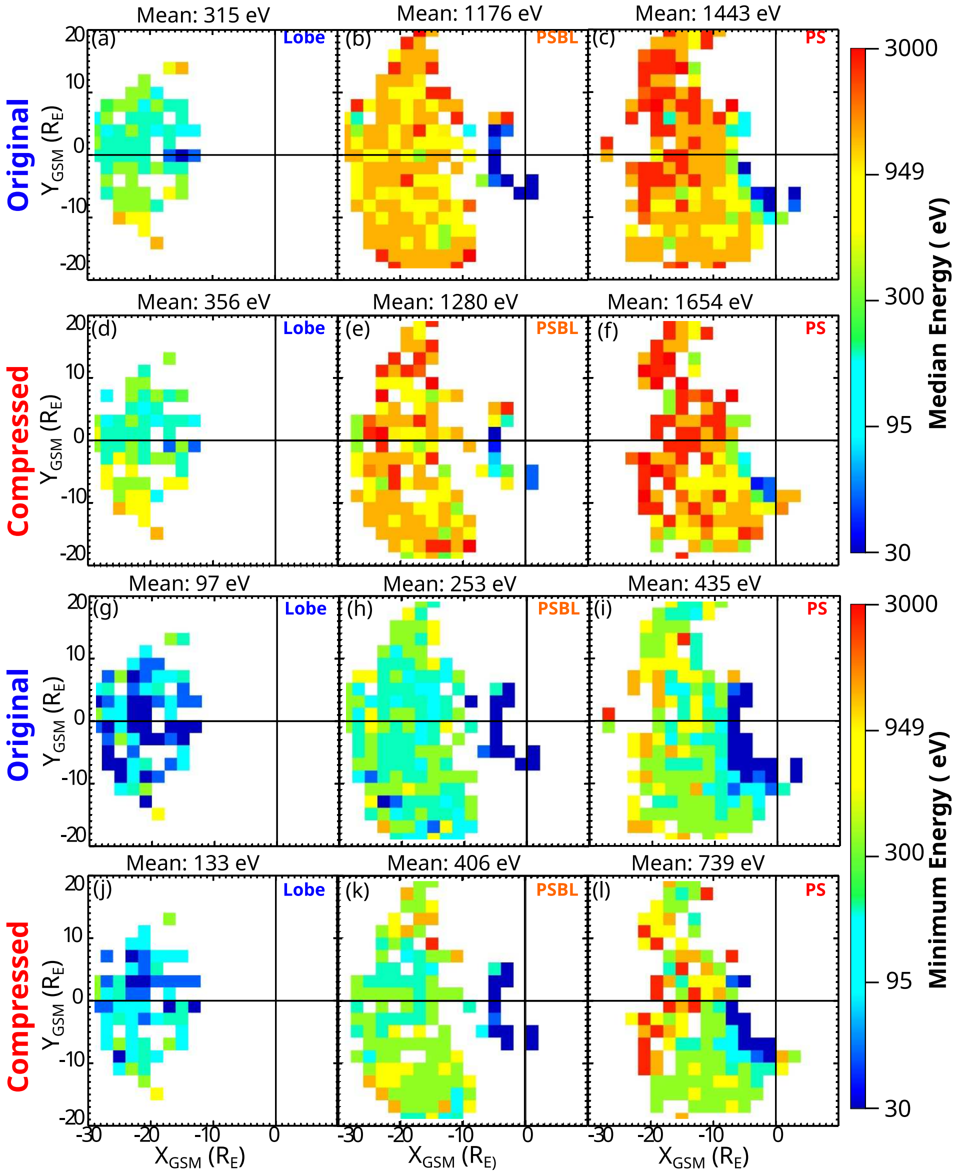

Figure A4. Median energy maps without (1st row) and with (2nd row) simulated compression, and minimum energy maps without (3rd row) and with (4th row) simulated compression. Columns from left to right are in lobes, the PSBL, and the PS. The numbers are the averaged value of the energy in each map. Data collected during the non-compression time during 2018–2019.

analyzer has a fixed dE/E and therefore the smaller the observed energy the smaller the dE for a certain geometric factor), Figure A3 shows the calculated correction factors as a function of energy for the different regions. This group of factors are applied to the occurrence frequency maps in Figure 7 where the maps are presented as a function of energy range as well.

We also studied the compression scheme's impact on the median and minimum energy maps. Figure A4 shows the comparisons of the observed median energy (top two rows) and minimum energy (bottom two rows) maps with and without the simulated compression scheme, with data collected during the non-compression time during 2018–2019. Maps are split into different regions in the three columns: lobe, PSBL, and PS. The numbers above each map indicate the averaged value of the energy in each map. The median energy maps present the mean value of the energies of all streaming O^+ identified in one grid. Comparison of median energy maps of streaming O^+ using data without compression (1st row of Figure A4) and with simulated compression (2nd row of Figure A4) shows that, in all regions, the median value of the energy is higher when the data is compressed. The increase is

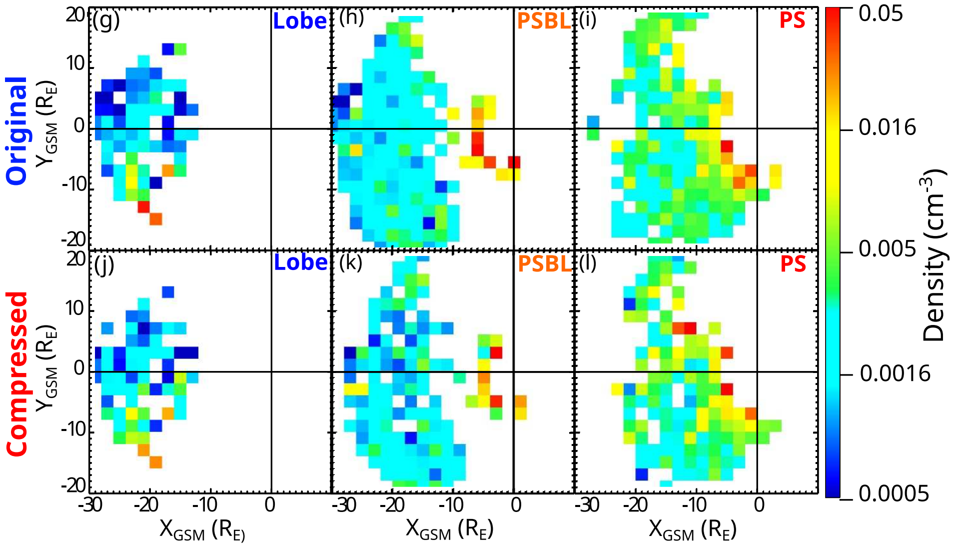

Figure A5. Median density maps without (1st row) and with (2nd row) simulated compression. Columns from left to right are in lobes, the PSBL, and the PS. The numbers are the averaged value of the energy in each map. Data collected during the non-compression time during 2018–2019.

smallest for lobes and the highest in the PS. However, the general patterns remain the same for the median energy maps for all regions. The minimum energy maps show the minimum value of the energy of all streaming O$^+$ observed in one bin. There is a clear increase in the minimum energy when data is compressed (4th row of Figure A4). The increase is smaller in the lobes (Figure A4j) and larger in the more isotropic regions (Figures A4k–A4l). In the PSBL and PS maps, the population near the Earth with energy around or lower than 30 eV remained in Figures A4k and A4l. The energy spatial profile is similar with and without compression. The count rate in the instrument is proportional to the energy flux, so the count rate is much lower for the low energy data than energetic data. As a result, the compression scheme that drops all the single-count data has a greater impact on the low-energy channels. When low-energy streaming O$^+$ ions are missing, the aggregated median energy is higher, and the observed minimum energy is much higher. Because the streaming population is anisotropic inside the lobes and gets scattered as it enters the denser part of the magnetosphere, the lobe streaming O$^+$ is less impacted by the compression scheme than the streaming O$^+$ in the PSBL and the PS. Due to the high density of the near-Earth nightside streaming O$^+$, their profile remains in the energy maps.

Figure A5 shows the comparison between the original density maps and those after compression, with same data as earlier comparisons. The compression scheme does not have a strong impact on the density maps for streaming O$^+$. Both the median values and the patterns remain with the compression scheme on. While the density effect is not large for the anisotropic beam populations analyzed in this study, the average effect on O$^+$ in the isotropic PS population is a factor of 10 and can be as high as a factor of 100.

Data Availability Statement

The csv data used of the streaming O$^+$ extracted and associated processed data in the study are available at via https://doi.org/10.5281/zenodo.10815490 with Creative Commons Attribution 4.0 International (Liao et al., 2024). The IDL software mms_oplus_beam, developed to extract streaming O$^+$, calculate its properties, and record relevant external data, as well as csv data set creation and visualization, is preserved at https://doi.org/10.5281/zenodo.11225963, via Creative Commons Attribution 4.0 International and developed using IDL programming language (Liao, 2024).

Acknowledgments
The work at the University of New Hampshire is supported by the NASA GI MMS 80NSSC17K0643, the NASA LWS 80NSSC19K0073, the NSF ANSWERS 2149787 and NSF GEM 2247712. The authors thank Jerry Goldstein for providing invaluable insights about spacecraft potential impact.

References

Angelopoulos, V., Kennel, C. F., Coroniti, F. V., Pellat, R., Spence, H. E., Kivelson, M. G., et al. (1993). Characteristics of ion flow in the quiet state of the inner plasma sheet. *Geophysical Research Letters*, *20*(16), 1711–1714. https://doi.org/10.1029/93GL00847

Arvelius, S., Yamauchi, M., Nilsson, H., Lundin, R., Hobara, Y., Rème, H., et al. (2005). Statistics of high-altitude and high-latitude O$^+$ ion outflows observed by Cluster/CIS. *Annales Geophysicae*, *23*(5), 1909–1916. https://doi.org/10.5194/angeo-23-1909-2005

Chappell, C. R., Moore, T. E., & Waite, J. H. (1987). The ionosphere as a fully adequate source of plasma for the Earth's magnetosphere. *Journal of Geophysical Research*, *92*(A6), 5896–5910. https://doi.org/10.1029/JA092iA06p05896

Chen, M. W., Wang, C.-P., Schulz, M., & Lyons, L. R. (2007). Solar-wind influence on MLT dependence of plasma sheet conditions and their effects on storm time ring current formation. *Geophysical Research Letters*, *34*(14), L14112. https://doi.org/10.1029/2007GL030189

Chong, G. S., Pitkänen, T., Hamrin, M., & Schillings, A. (2021). Ion convection as a function of distance to the neutral sheet in earth's magnetotail. *Journal of Geophysical Research: Space Physics*, *126*(12). https://doi.org/10.1029/2021JA029694

Cladis, J. B. (1986). Parallel acceleration and transport of ions from polar ionosphere to plasma sheet. *Geophysical Research Letters*, *13*(9), 893–896. https://doi.org/10.1029/GL013i009p00893

Cully, C. M., Donovan, E. F., Yau, A. W., & Arkos, G. G. (2003). Akebono/Suprathermal mass spectrometer observations of low-energy ion outflow: Dependence on magnetic activity and solar wind conditions. *Journal of Geophysical Research*, *108*(A2), 2001JA009200. https://doi.org/10.1029/2001JA009200

Elliott, H. A., Comfort, R. H., Craven, P. D., Chandler, M. O., & Moore, T. E. (2001). Solar wind influence on the oxygen content of ion outflow in the high-altitude polar cap during solar minimum conditions. *Journal of Geophysical Research*, *106*(A4), 6067–6084. https://doi.org/10.1029/2000JA003022

Engwall, E., Eriksson, A. I., Cully, C. M., André, M., Torbert, R., & Vaith, H. (2009). Earth's ionospheric outflow dominated by hidden cold plasma. *Nature Geoscience*, *2*(1), 24–27. https://doi.org/10.1038/ngeo387

Gkioulidou, M., Ohtani, S., Ukhorskiy, A. Y., Mitchell, D. G., Takahashi, K., Spence, H. E., et al. (2019). Low-energy (<keV) O^+ ion outflow directly into the inner magnetosphere: Van Allen probes observations. *Journal of Geophysical Research: Space Physics*, *124*(1), 405–419. https://doi.org/10.1029/2018JA025862

Goldstein, J., Burch, J. L., Fuselier, S. A., Gomez, R., Gonzalez, C. A., Kim, M. J., et al. (2023). MMS observations of dayside warm (several eV to 100 eV) ions in the middle and outer magnetosphere. *Journal of Geophysical Research: Space Physics*, *128*(3), e2022JA031051. https://doi.org/10.1029/2022JA031051

Haaland, S., Paschmann, G., Förster, M., Quinn, J., Torbert, R., Vaith, H., et al. (2008). Plasma convection in the magnetotail lobes: Statistical results from cluster EDI measurements. *Annales Geophysicae*, *26*(8), 2371–2382. https://doi.org/10.5194/angeo-26-2371-2008

Huddleston, M. M., Chappell, C. R., Delcourt, D. C., Moore, T. E., Giles, B. L., & Chandler, M. O. (2005). An examination of the process and magnitude of ionospheric plasma supply to the magnetosphere. *Journal of Geophysical Research*, *110*(A12), A12202. https://doi.org/10.1029/2004JA010401

Hull, A. J., Chaston, C. C., Bonnell, J. W., Wygant, J. R., Kletzing, C. A., Reeves, G. D., & Gerrard, A. (2019). Dispersive alfvén wave control of O^+ ion outflow and energy densities in the inner magnetosphere. *Geophysical Research Letters*, *46*(15), 8597–8606. https://doi.org/10.1029/2019GL083808

Juusola, L., Østgaard, N., & Tanskanen, E. (2011). Statistics of plasma sheet convection: PS statistics. *Journal of Geophysical Research: Space Physics*, *116*(A8). https://doi.org/10.1029/2011JA016479

Juusola, L., Østgaard, N., Tanskanen, E., Partamies, N., & Snekvik, K. (2011). Earthward plasma sheet flows during substorm phases: PS flows during substorms. *Journal of Geophysical Research*, *116*(A10). https://doi.org/10.1029/2011JA016852

Keika, K., Kistler, L. M., & Brandt, P. C. (2013). Energization of O^+ ions in the earth's inner magnetosphere and the effects on ring current buildup: A review of previous observations and possible mechanisms: A review of O^+ energization. *Journal of Geophysical Research: Space Physics*, *118*(7), 4441–4464. https://doi.org/10.1002/jgra.50371

King, J. H., & Papitashvili, N. E. (2020). OMNI 1-min data set [Dataset]. *NASA Space Physics Data Facility*. https://doi.org/10.48322/45BB-8792

Kistler, L. M., Ipavich, F. M., Hamilton, D. C., Gloeckler, G., Wilken, B., Kremser, G., & Stüdemann, W. (1989). Energy spectra of the major ion species in the ring current during geomagnetic storms. *Journal of Geophysical Research*, *94*(A4), 3579–3599. https://doi.org/10.1029/JA094iA04p03579

Kistler, L. M., & Mouikis, C. G. (2016). The inner magnetosphere ion composition and local time distribution over a solar cycle: Cluster Ion Composition. *Journal of Geophysical Research: Space Physics*, *121*(3), 2009–2032. https://doi.org/10.1002/2015JA021883

Kistler, L. M., Mouikis, C. G., Asamura, K., Yokota, S., Kasahara, S., Miyoshi, Y., et al. (2019). Cusp and nightside auroral sources of O^+ in the plasma sheet. *Journal of Geophysical Research: Space Physics*, *124*(12), 10036–10047. https://doi.org/10.1029/2019JA027061

Kistler, L. M., Mouikis, C. G., Cao, X., Frey, H., Klecker, B., Dandouras, I., et al. (2006). Ion composition and pressure changes in storm time and nonstorm substorms in the vicinity of the near-Earth neutral line. *Journal of Geophysical Research*, *111*(A11), A11222. https://doi.org/10.1029/2006JA011939

Kistler, L. M., Mouikis, C. G., Klecker, B., & Dandouras, I. (2010). Cusp as a source for oxygen in the plasma sheet during geomagnetic storms: Oxygen in the plasma sheet-cusp source. *Journal of Geophysical Research*, *115*(A3). https://doi.org/10.1029/2009JA014838

Kistler, L. M., Mouikis, C. G., Spence, H. E., Menz, A. M., Skoug, R. M., Funsten, H. O., et al. (2016). The source of O^+ in the storm time ring current. *Journal of Geophysical Research: Space Physics*, *121*(6), 5333–5349. https://doi.org/10.1002/2015JA022204

Liao, J. (2011). *Statistical study of oxygen transport from the cusp to the plasmasheet*. Doctoral Dissertations. Retrieved from https://scholars.unh.edu/dissertation/642

Liao, J. (2024). shihikoo/mms_oplus_beam: V 1.0.0 (Version v1.0.0) [Software]. *Zenodo*. https://doi.org/10.5281/ZENODO.11225963

Liao, J., Kistler, L., & Mouikis, C. (2024). Streaming O+ data from MMS/HPCA [Dataset]. *Zenodo*. https://doi.org/10.5281/ZENODO.10815490

Liao, J., Kistler, L. M., Mouikis, C. G., Klecker, B., Dandouras, I., & Zhang, J.-C. (2010). Statistical study of O^+ transport from the cusp to the lobes with cluster CODIF data: O^+ transport statistical study. *Journal of Geophysical Research*, *115*(A12). https://doi.org/10.1029/2010JA015613

Liu, Z.-Y., & Zong, Q.-G. (2022). Ionospheric oxygen outflows directly injected into the inner magnetosphere: Van Allen probes statistics. *Journal of Geophysical Research: Space Physics*, *127*(10). https://doi.org/10.1029/2022JA030611

Maggiolo, R., & Kistler, L. M. (2014). Spatial variation in the plasma sheet composition: Dependence on geomagnetic and solar activity: O+ and H+ density in the plasmasheet. *Journal of Geophysical Research: Space Physics*, *119*(4), 2836–2857. https://doi.org/10.1002/2013JA019517

Matzka, J., Bronkalla, O., Tornow, K., Elger, K., & Stolle, C. (2021). Geomagnetic Kp index (version 1.0). https://doi.org/10.5880/KP.0001

Miyashita, Y., Seki, K., Sakaguchi, K., Hiraki, Y., Nosé, M., Machida, S., et al. (2020). On the transition between the inner and outer plasma sheet in the earth's magnetotail. *Journal of Geophysical Research: Space Physics*, *125*(4). https://doi.org/10.1029/2019JA027561

Moore, T. E., Chandler, M. O., Chappell, C. R., Comfort, R. H., Craven, P. D., Delcourt, D. C., et al. (1999). Polar/TIDE results on polar ion outflows. In L. Burch, L. Carovillano, & K. Antiochos (Eds.), *Geophysical monograph series* (Vol. 109, pp. 87–101). American Geophysical Union. https://doi.org/10.1029/GM109p0087

Moore, T. E., Fok, M.-C., Christon, S. P., Chen, S.-H., Chandler, M. O., Delcourt, D. C., et al. (2005). Solar and ionospheric plasmas in the ring current region. In J. Burch, M. Schulz, & H. Spence (Eds.), *Geophysical monograph series* (Vol. 159, pp. 179–194). American Geophysical Union. https://doi.org/10.1029/159GM14

Moore, T. E., Peterson, W. K., Russell, C. T., Chandler, M. O., Collier, M. R., Collin, H. L., et al. (1999). Ionospheric mass ejection in response to a CME. *Geophysical Research Letters*, *26*(15), 2339–2342. https://doi.org/10.1029/1999GL900456

Mouikis, C. G., Kistler, L. M., Liu, Y. H., Klecker, B., Korth, A., & Dandouras, I. (2010). H^+ and O^+ content of the plasma sheet at 15-19 Re as a function of geomagnetic and solar activity: The plasma sheet H^+ and O^+ content. *Journal of Geophysical Research*, *115*(A12). https://doi.org/10.1029/2010JA015978

Nosé, M., Keika, K., Kletzing, C. A., Spence, H. E., Smith, C. W., MacDowall, R. J., et al. (2016). Van Allen Probes observations of magnetic field dipolarization and its associated O^+ flux variations in the inner magnetosphere at $L < 6.6$. *Journal of Geophysical Research: Space Physics*, *121*(8), 7572–7589. https://doi.org/10.1002/2016JA022549

Nosé, M., Matsuoka, A., Miyoshi, Y., Asamura, K., Hori, T., Teramoto, M., et al. (2022). Flux enhancements of field-aligned low-energy O^+ ion (FALEO) in the inner magnetosphere: A possible source of warm plasma cloak and oxygen torus. *Journal of Geophysical Research: Space Physics*, *127*(3), e2021JA030008. https://doi.org/10.1029/2021JA030008

Nosé, M., McEntire, R. W., & Christon, S. P. (2003). Change of the plasma sheet ion composition during magnetic storm development observed by the Geotail spacecraft. *Journal of Geophysical Research*, *108*(A5), 2002JA009660. https://doi.org/10.1029/2002JA009660

Nosé, M., Sugiura, M., Kamei, T., Iyemori, T., & Koyama, Y. (2015). Dst index. *WDC for Geomagnetism*. https://doi.org/10.17593/14515-74000

Nowrouzi, N., Kistler, L. M., Zhao, K., Lund, E. J., Mouikis, C., Payne, G., & Klecker, B. (2023). The variation of ionospheric O^+ and H^+ outflow on storm timescales. *Journal of Geophysical Research: Space Physics*, *128*(11), e2023JA031786. https://doi.org/10.1029/2023JA031786

Sauvaud, J.-A., Louarn, P., Fruit, G., Stenuit, H., Vallat, C., Dandouras, J., et al. (2004). Case studies of the dynamics of ionospheric ions in the Earth's magnetotail. *Journal of Geophysical Research*, *109*(A1), A01212. https://doi.org/10.1029/2003JA009996

Seki, K., Elphic, R. C., Thomsen, M. F., Bonnell, J., Lund, E. J., Hirahara, M., et al. (2000). Cold flowing O^+ beams in the lobe/mantle at Geotail: Does FAST observe the source? *Journal of Geophysical Research*, *105*(A7), 15931–15944. https://doi.org/10.1029/1999JA900470

Seki, K., Elphic, R. C., Thomsen, M. F., Bonnell, J., McFadden, J. P., Lund, E. J., et al. (2002). A new perspective on plasma supply mechanisms to the magnetotail from a statistical comparison of dayside mirroring O^+ at low altitudes with lobe/mantle beams. *Journal of Geophysical Research: Space Physics*, *107*(A4). https://doi.org/10.1029/2001JA900122

Strangeway, R. J., Ergun, R. E., Su, Y.-J., Carlson, C. W., & Elphic, R. C. (2005). Factors controlling ionospheric outflows as observed at intermediate altitudes. *Journal of Geophysical Research: Space Physics*, *110*(A3). https://doi.org/10.1029/2004JA010829

Torbert, R. B., Russell, C. T., Magnes, W., Ergun, R. E., Lindqvist, P.-A., LeContel, O., et al. (2016). The FIELDS instrument suite on MMS: Scientific objectives, measurements, and data products. *Space Science Reviews*, *199*(1–4), 105–135. https://doi.org/10.1007/s11214-014-0109-8

Yao, A. W., Abe, T., André, M., Howarth, A. D., & Peterson, W. K. (2021). Ionospheric ion acceleration and transport. In R. Maggiolo, N. André, H. Hasegawa, D. T. Welling, Y. Zhang, & L. J. Paxton (Eds.), *Geophysical monograph series* (1st ed., pp. 207–217). Wiley. https://doi.org/10.1002/9781119815624.ch14

Young, D. T., Burch, J. L., Gomez, R. G., De Los Santos, A., Miller, G. P., Wilson, P., et al. (2016). Hot plasma composition analyzer for the magnetospheric Multiscale mission. *Space Science Reviews*, *199*(1–4), 407–470. https://doi.org/10.1007/s11214-014-0119-6

Zhao, K., Kistler, L. M., Lund, E. J., Nowrouzi, N., Kitamura, N., & Strangeway, R. J. (2020). Factors controlling O^+ and H^+ outflow in the cusp during a geomagnetic storm: FAST/TEAMS observations. *Geophysical Research Letters*, *47*(11), e2020GL086975. https://doi.org/10.1029/2020GL086975

Zhao, K., Kistler, L. M., Lund, E. J., Nowrouzi, N., Kitamura, N., & Strangeway, R. J. (2022). Nightside auroral H^+ and O^+ outflows versus energy inputs during a geomagnetic storm. *Journal of Geophysical Research: Space Physics*, *127*(11). https://doi.org/10.1029/2022JA030923